



HAL
open science

Experimental constraints on the behaviour of sulphur in the 2021 Cumbre Vieja (La Palma) basanite

Diletta Frascerra, Bruno Scaillet, Joan Andújar, Clive Oppenheimer, Stéphane Scaillet, Joan Martí, Ramón Casillas, Carmen López

► **To cite this version:**

Diletta Frascerra, Bruno Scaillet, Joan Andújar, Clive Oppenheimer, Stéphane Scaillet, et al.. Experimental constraints on the behaviour of sulphur in the 2021 Cumbre Vieja (La Palma) basanite. *Journal of Volcanology and Geothermal Research*, 2024, 456, <10.1016/j.jvolgeores.2024.108219>. <insu-04796214>

HAL Id: insu-04796214

<https://insu.hal.science/insu-04796214v1>

Submitted on 5 Dec 2024

HAL is a multi-disciplinary open access archive for the deposit and dissemination of scientific research documents, whether they are published or not. The documents may come from teaching and research institutions in France or abroad, or from public or private research centers.

L'archive ouverte pluridisciplinaire **HAL**, est destinée au dépôt et à la diffusion de documents scientifiques de niveau recherche, publiés ou non, émanant des établissements d'enseignement et de recherche français ou étrangers, des laboratoires publics ou privés.



Distributed under a Creative Commons CC BY 4.0 - Attribution - International License

Experimental constraints on the behaviour of sulphur in the 2021 Cumbre Vieja (La Palma) basanite

Diletta Frascerra^{1*}, Bruno Scaillet¹, Joan Andújar¹, Clive Oppenheimer², Stéphane Scaillet¹, Joan Martí³, Ramón Casillas⁴, Carmen López⁵.

¹Institut des Sciences de la Terre d'Orléans, UMR 7327, CNRS–Université d'Orléans–BRGM (France).

²Department of Geography, University of Cambridge (UK).

³Dep. of Geosciences, IDAEA-CSIC, Barcelona, Spain.

⁴ Department of Earth Sciences, Universidad de la Laguna, Tenerife, Spain

⁵ IGN, Madrid, Spain.

*Corresponding author: diletta.frascerra@univ-orleans.fr

Abstract. We performed experiments to constrain the effects of sulphur and oxygen fugacities on magma chamber and outgassing conditions of the La Palma 2021 eruption. Based on a series of controlled experiments on basanitic products carried out at 1040°C and 200 MPa, we show that sulphur addition affects the stabilities of amphibole and olivine, in particular at high fO_2 and elevated S contents which together inhibit amphibole crystallization. We also show that the overriding control on S systematics is oxygen fugacity, with melts capable of dissolving from 1000 up to 8000 ppm S, depending on fO_2 . Increasing the bulk S content increases the S content of the silicate melt up to ~ 2000 ppm for $fO_2 < NNO+2$, and 7000–8000 ppm at higher fO_2 . Further increase in dissolved S is prevented by the buffering effects of either sulphide at low fO_2 or anhydrite at high fO_2 . Modelling shows that the observed CO_2/SO_2 and H_2O/SO_2 ratios of volcanic gas emissions during the eruption imply a pre-existing > 5 wt% exsolved fluid in the reservoir, with fS_2 at ~ 0.1 MPa at fO_2 above NNO. Our work confirms that basaltic magmas may coexist with a significant amount of excess fluid which in turn holds an important part of the sulfur budget emitted to the atmosphere.

Keywords: La Palma, sulphur solubility, basanite, sulphur degassing

1. Introduction

The 2021 Cumbre Vieja eruption on La Palma produced ~ 0.2 km³ of alkali basalt over a three month period, with devastating impacts on the built environment and agricultural land (Bonadonna et al., 2022; Del Fresno et al., 2023a; González et al., 2019; Ubide et al., 2023; Dayton et al., 2024). La Palma is made up of two volcanic centres. The oldest is the Taburiente centre in the north and the presently active Cumbre Vieja centre in the south of the island (Carracedo et al., 2001 and references therein). The volcanic activity of Cumbre Vieja area began about 123,000 years ago, and its complex extends from N to S being mainly composed of single eruptive centers spread along fissures. The eruptive products belong to the alkaline series, with emission of alkaline basalts, basanites, trachybasalts, tephrites and phonolites (e.g., Carracedo et al., 2001). Prior to the 2021 eruption, several eruptions have been recorded over the last 500 years (about 8), all associated with explosive events on the summit, and effusive lava flows along the flanks (Carracedo et al., 2001). La Palma is part of the oceanic island basalt system of the Canary Islands, which is fed by a hotspot of presumed mantle origin probably influenced by the rotation of the African plate (e.g., Day et al. 2022 and references therein).

42 The 2021 eruption was accompanied by vigorous degassing of CO₂ and S gas species, which were measured
 43 intermittently using a variety of sensors (e.g., Burton et al., 2023). Estimates of the quantity of the total SO₂
 44 emitted range from 1 to over 4 Tg (Albertos et al., 2023; Burton et al., 2023; Dayton et al., 2024; Hayer et
 45 al., 2022). Melt inclusion analyses reveal an average pre-eruptive S content of ~ 3000 ppm (Castro and
 46 Feisel, 2022; Burton et al., 2023; Dayton et al., 2024). Complete syneruptive degassing of this sulphur would
 47 yield over 3 Tg of SO₂, i.e., an amount within the range of estimated emissions. However, estimates of initial
 48 CO₂ contents lie in the range 3–5 wt% (Burton et al., 2023), which is more than sufficient to saturate a
 49 basanite magma (e.g. Jiménez-Mejías et al., 2021; Lo Forte et al., 2024) at crustal pressures (<1 GPa). Given
 50 the likelihood of a pre-eruptive gas phase in the reservoir (Sandoval-Velasquez et al., 2023; Zanon et al.,
 51 2024; Dayton et al., 2024) raises the question of how much sulphur was partitioned into it? In silicic magmas,
 52 S is inferred to reside dominantly in the gas phase (e.g. Scaillet et al., 1998; Keppler, 1999).

53 Critical to understanding the behaviour of S in magmatic systems is to constrain their redox state or oxygen
 54 fugacity (fO_2), which exerts a major control on S solubility and partitioning (e.g., (Carroll and Rutherford,
 55 1988; Luhr, 1990; Scaillet et al., 1998; Jugo, 2004; Moretti and Ottonello, 2005; O’Neill, 2021; Boulliang
 56 and Wood, 2023; Hughes et al., 2023). Knowing whether S goes into the fluid/gas or not is crucial for
 57 interpreting the composition of volcanic gases at the surface, which are routinely measured for the purposes
 58 of hazard assessment.

59 Our overall aim here is to develop understanding of S solubility and partitioning in mafic magmas with
 60 hotspot and ocean-island basalt (OIB) affinities through a set of experiments on La Palma 2021 basanite in
 61 which fO_2 and the amount of S were varied. To this end, we reconstructed eruptive conditions at La Palma.
 62 In particular, we focused on the amount of sulphur and its fugacity at pre-eruptive conditions in the reservoir
 63 and in the fluid phase during eruptive outgassing.

64 2. Experimental technique

65 2.1 Starting material and apparatus

66 Basanite lapilli (1 Top/27-9-2021) from the 2021 eruption of La Palma were selected as the starting
 67 material. The lapilli were finely ground using an agate mortar and then melted in a Pt crucible at
 68 1400°C for 4 h at atmospheric pressure. These steps were repeated to obtain an homogeneous and
 69 anhydrous glass. Homogeneity was verified using the Electron Micro Probe analyzer (EMPA). The
 70 composition of the glass is reported in Table 1.

71 The experiments were performed with Internally Heated Pressure Vessels (IHPV) at the Institut
 72 des Sciences de la Terre d’Orléans (ISTO), using as pressure media either Ar or a H₂-Ar mixture
 73 gas (Scaillet et al., 1992). Up to eight gold capsules were placed in a ceramic sample holder, which
 74 was suspended between two type-S thermocouples with a Pt or Rh wire, depending on the redox
 75 conditions. During the experiments, we maintained a thermal gradient of less than 10 °C between
 76 the top and the bottom thermocouples. All experiments concluded with a rapid drop quench with
 77 cooling rates of order 100°C/s (Di Carlo et al., 2006).

78

SiO ₂	TiO ₂	Al ₂ O ₃	FeO	MnO	MgO	CaO	Na ₂ O	K ₂ O	P ₂ O ₅	Cl	S	Total
44.11	3.83	14.42	12.22	0.18	7.49	10.92	4.05	1.73	0.97	0.01	0.01	97.75
(0.26)	(0.10)	(0.13)	(0.26)	(0.05)	(0.05)	(0.11)	(0.08)	(0.10)	(0.07)	(0.01)	(0.01)	

79 *Table 1 Composition starting material*

80 2.2 Capsule preparation and experimental conditions

81 The finely ground starting material was divided into three batches. Two S-bearing batches were
82 prepared either by adding 2 wt.% native sulphur or 3 wt.% pyrrhotite (corresponding to 1.1 wt.%
83 sulphur) and the third batch was left S-free. These bulk sulphur contents are above the sulphur
84 solubility of basaltic melts under our experimental conditions (e.g. Moune et al. 2009; Luhr, 1990).
85 Hence, when using the S-bearing batches directly (i.e. without mixing them with the S-free batch)
86 as a starting material, the bulk content of sulphur should promote saturation in either sulphide or
87 sulphate unless the coexisting fluid scavenges sulphur (see results).

88 For each experiment, six to seven Au capsules were prepared (inner and outer diameter of 2.5–2.9
89 mm, height of 1.5 cm). Gold was used to minimize the loss of sulphur and iron. Capsules were
90 loaded first with 3 mg of deionized water to ensure fluid saturation of the system (corresponding
91 to about 5 wt% dissolved H₂O at 200 MPa at H₂O saturation, e.g. Jiménez-Mejías et al. (2021)),
92 then with 30 mg of silicate powder prepared by mixing S- or FeS-doped powder with S-free glass
93 in various proportions to obtain different concentrations of sulphur (Table 2). In the following, we
94 refer to these two series as S-doped or FeS-doped charges. The weight of the capsules was measured
95 after welding, then after a test in an oven at 125 °C for at least 1 h, and finally after the experiment
96 to check for volatile leaks. Only charges with a difference of less than 0.0003 g were considered
97 successful. Considering the context of La Palma 2021 eruption as summarised above, it would have
98 been interesting to add CO₂ as a fluid component. This however would have needed to raise the
99 temperature of the experiments which would have in turn prohibited the use of Au containers:
100 Containers made of either Pt or of AuPd alloys are prone to significant alteration by sulphur, which
101 severely complicates the interpretation of results.

102 All the experiments were run at 1040 °C and 200 MPa but with variable fO_2 (between NNO-0.48
103 and NNO+4.1), controlled by sensors of NiPd for experiments above NNO and CoPd for
104 experiments below NNO (Taylor et al., 1992; Table 2). The fS_2 of pyrrhotite-bearing charges was
105 calculated following Froese and Gunter (1976).

106 On-going experiments aimed at determining pre-eruptive conditions of La Palma basalts (Andújar
107 et al., submitted) suggest storage conditions of early erupted magmas at somewhat higher P and T
108 (i.e., 300 MPa, 1060–1080°C). A number of petrological studies have shown that latter erupted
109 magmas record higher pressures, >500 MPa, and temperatures above 1100°C (e.g., Castro and
110 Feisel, 2022; Day et al., 2022; Ubide et al., 2023; Dayton et al., 2024). The reason of choice of our
111 P-T conditions is essentially practical. As stressed above, the lower temperature allows us to use
112 Au capsules, which considerably limits S loss from the melt+fluid towards the capsule (and also
113 that of Fe loss), compared to either AuPd or Pt capsules, maintaining the physical integrity of
114 containers. Such a low temperature is achieved by working with elevated melt water contents,
115 which depress liquidus temperatures significantly in basaltic systems while maintaining the
116 composition of near liquidus residual melts broadly basaltic (e.g., Sisson and Grove, 1993).
117 Performing experiments at 300 MPa would have been possible, but the higher water content of the
118 basaltic melts (>7 wt%) at this pressure renders those liquid poorly quenchable, even with drop

119 quench technique. Therefore, given the H₂O-rich conditions of our experiments, we decided to
120 perform the experiments at 200 MPa, with the objective of favouring the solubility of the sulphur
121 and facilitating the quench of the glass. Nevertheless, we recognise the potential for this approach
122 to result in differences with the natural system, in particular a higher proportion of amphibole
123 relative to what is observed in the rocks. Higher temperatures will also affect the solubility of
124 sulphur: for instance an increase of 50°C in the fO_2 range NNO - NNO+1.5 increases the S
125 solubility by 10-30%, if fS_2 is kept constant (e.g., Boulliang and Wood, 2023).

126

127 **3. Analytical methods**

128 *3.1 Analytical techniques*

129 Half of the recovered run products were embedded in epoxy and polished for optical inspection
130 and, then carbon-coating, for scanning electron microscopy (SEM) using the Zeiss FEG of ISTO
131 to identify phases, including those of quench origin.

132 Glass and minerals were analysed using a Cameca SX FIVE EMPA (CNRS-Université d'Orléans-
133 BRGM). The analytical conditions were 15 kV, 10 nA and a peak count time of 10 s. Glasses were
134 analysed with a defocused beam of 5, 10 or 20 μ m, depending on the size of the available glass
135 pools. Sulphur was determined using an LPET crystal and a 20 s counting time. A focused beam
136 was used for the minerals. Sulphides were analysed during separate sessions with the following
137 analytical conditions: 20 kV and 50 nA, using PET and LPET crystals for S, an acquisition time of
138 30 s, while Fe was analyzed with LIF and LLIF crystals. The Ni and Cu had acquisition times of
139 10s. In addition, Si was used to detect possible glass contamination. At the beginning and end of
140 the analytical session, two synthetic pyrrhotites of known compositions (as determined by X-ray
141 analyses, (Clemente et al., 2004), Po5 and Po7, were analysed to check the stability of the
142 calibration.

143 Three glasses with different sulphur concentrations were synthesised at 1200°C using the same
144 experimental apparatus and starting glass. The sulphur concentrations measured by the microprobe
145 were found to differ by less than 100 ppm relative to the added amount, validating our analytical
146 procedure for measuring S.

147 The H₂O concentration in the run products was estimated following Devine et al.(1995), analyzing
148 at the beginning and end of each analytical session standard basaltic glasses of known water
149 contents (F1c, F05, F3c2 and F2b, in Jiménez-Mejías et al. (2021)).

150 *3.2 Mass balance and ImageJ software calculations*

151 The proportion of each phase was calculated by mass balance using a constrained least-squares
152 model with the propagation of analytical errors of the experimental phases (Albarède, 1996; Scaillet
153 and Evans, 1999). The proportion of glass was also calculated by processing SEM images at 100
154 μ m magnification using ImageJ software, on a vesicle-free basis.

155 The amount of sulphur in the coexisting fluid phase was estimated by mass balance, i.e. by
156 subtracting the masses of S in sulphur-bearing phases (glass, sulphide, sulphate) from the initial
157 mass of sulphur, taking into account the phase percentages as calculated above. The S wt% was
158 then calculated by determining the amount of H₂O in the fluid using the same method (Table 2).

159

Run	P (MPa)	T (°C)	Time (min)	Δ NNO	log fO ₂	log fS ₂ (bar)	H ₂ O&	S% and type loaded	S wt% Glass	S wt% Fluid	Mineral assemblage
lpm 1	200	1040	960	1.34	8.40	0.28	4.1	2%-native	0.22 (0.02)	9.2	Ol-Amph-Px- FeS
lpm 2						-0.24	1.8	1%-native	0.11 (0.01)	5.2	Ol-Amph-Px - Mt-FeS
lpm 33						-	4.0	0.5%-native	0.18 (0.01)	5.4	Ol -Amph - Px - Mt
lpm 4						-0.24	3.1	1.12%-FeS	0.23 (0.01)	5.1	Ol-Amph-Px- Mt-FeS
lpm 5						-	4.1	0.56%-FeS	0.21 (0.03)	6.3	Ol - Amph-Px -Mt
lpm 6						-	5.9	0.28%-FeS	0.10 (0.02)	3.5	Ol-Amph-Px- Mt
lpm 34						-	4.5	0%S	-	-	Ol-Amph-Px- Mt
lpm 7	200	1040	960	2.38	7.37	-	3.8	2%-native	0.73 (0.04)	16.6	Ol-Mt-Ilm
lpm 8						-	4.7	1%-native	0.86 (0.06)	3.6	Ol-Px-Mt
lpm 9						-	3.9	0.5%-native	0.57 (0.03)	2.5	Ol-Amph-Px- Mt
lpm 13	200	1040	360	3.30	6.44	-	5.4	2%-native	0.75 (0.04)	21.1	Ol-Mt-Ilm
lpm 14						-	6.3	1%-native	0.75 (0.04)	13.3	Ol-Px-Mt
lpm 15						-	6.8	0.5%-native	0.65 (0.09)	--	Px-Mt
lpm 16						-	2.0	1.12%-FeS	0.79 (0.03)	6.9	Px-Mt-Ilm
lpm 17						-	6.1	0.56%-FeS	0.65 (0.09)	0.3	Ol-Px-Mt
lpm 18						-	6.5	0.28%-FeS	0.33 (0.03)	1.7	Amph-Px-Mt
lpm 19	200	1040	360	4.10	5.65	-	4.8	2%-native	0.68 (0.05)	-	Ol-Px-Mt- Ilm-Anhy
lpm 20						-	5.6	1%-native	0.64 (0.01)	9.3	Ol-Amph-Px- Mt-Ilm
lpm 21						-	4.5	0.5%-native	0.58 (0.05)	3.1	Amph-Px-Mt
lpm 22						-	5.2	1.12%-FeS	0.71 (0.04)	9.0	Ol-Px-Mt
lpm 23						-	5.8	0.56%-FeS	0.65 (0.03)	3.1	Amph-Px-Mt
lpm 24						-	6.4	0.28%-FeS	0.38 (0.03)	1.4	Amph-Px-Mt- Ap
lpm 25						-	4.6	0%S	-	-	Amph-Px-Mt
lpm 26	200	1040	360	-0.48	1023	-0.63	3.5	2%-native	0.12 (0.01)	3.7	Ol-Amph-Px- FeS
lpm 27						-1.59	2.4	1%-native	0.10 (0.01)	1.2	Ol-Amph-Px- FeS
lpm 28						-	3.1	0.5%-native	0.13 (0.01)	5.5	Ol-Amph-Px- Mt
lpm 29						-1.02	3.6	1.12%-FeS	0.19 (0.03)	6.7	Ol-FeS-Mt
lpm 30						-0.75	3.1	0.56%-FeS	0.19 (0.03)	3.7	Ol-Px-FeS
lpm 32						-	4.7	0%S	-	-	Ol-Amph?- Px-Mt

161 *Table 2 Experimental conditions, water and sulphur contents of quenched glass. H₂O is calculated with the method of Devine et al*
162 *(1996). The fS₂ is calculated using the method of Froese and Gunter (1976). Amph? = quench phase*

165 **4. Results**

166 The experiments generated different mineral assemblages, depending on fO_2 and the amount of S
 167 added, as shown in Fig. 1.

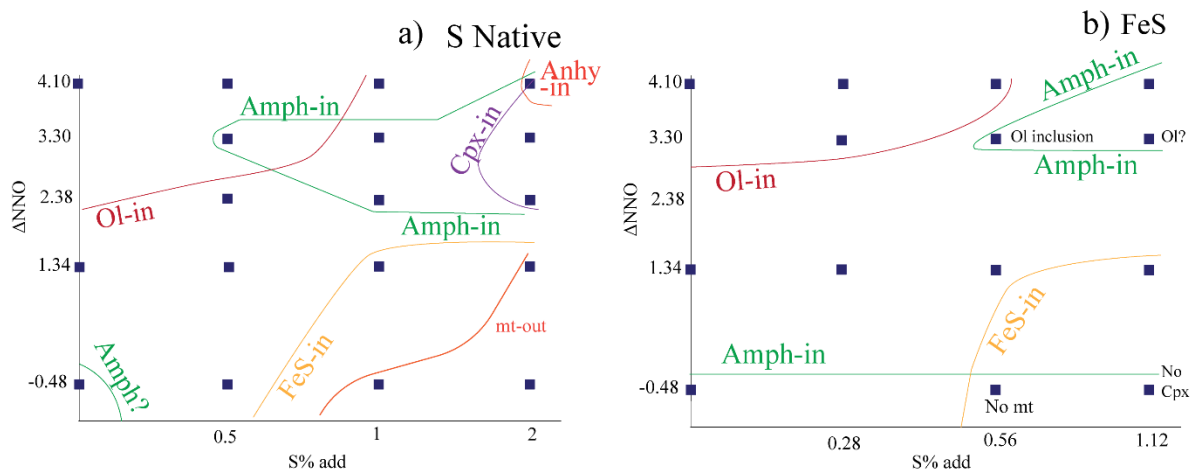


Fig. 1 Equilibrium phase diagram at 1040°C and 200 MPa for both S-doped (a) and FeS-doped (b) charges. Phases lie inside their stability field. Ol=olivine; Cpx= clinopyroxene; Amph = amphibole; Anhy = anhydrite; mt=magnetite.

168 In the S-doped series, anhydrite crystallizes at high fO_2 while pyrrhotite is present at low fO_2 . In
 169 detail, anhydrite is found only in the charge with 2 wt.% added S at NNO+4.1, while pyrrhotite is
 170 present with 1 wt.% and 2 wt.% S added at NNO+1.34 and NNO-0.48. Olivine occurs in almost
 171 every charge, except for those poorer in sulphur at high fO_2 . Apart from three charges with 2 wt.%
 172 S added at NNO+2.38, 3.3 and 4.1, pyroxene is present in all experimental charges. Amphibole
 173 distribution is more complex. It did not crystallise in charges with 2 wt.% and 1 wt.% S at
 174 NNO+2.38, in any experiments at NNO+3.3, in the charge at 2 wt.% S under the most oxidising
 175 conditions and in the S-free charge at NNO-0.48 (Fig.1a).

176 The phase diagram of the FeS-doped series is broadly similar. The stability range of olivine is
 177 almost identical, except that Ol was also found in the 0.56 wt.% S charge at NNO+4.10. In the
 178 sulphur-rich experiment at NNO+3.3, Ol was not found but owing to its low abundance in other
 179 charges, it may have been overlooked. In the charge *lpm 1-top+S17*, olivine is present as inclusions
 180 in the pyroxene. Pyroxene is present in all charges, except for that with 1.12 wt.% S at NNO-0.48.
 181 FeS has a similar stability field to that identified by the S-doped series, however it is absent at 0.56
 182 wt.% S and NNO+1.34. The amphibole field is also similar in S-doped case, except that it is not
 183 found at NNO-0.48 (Fig.1b).

184

185

186

187

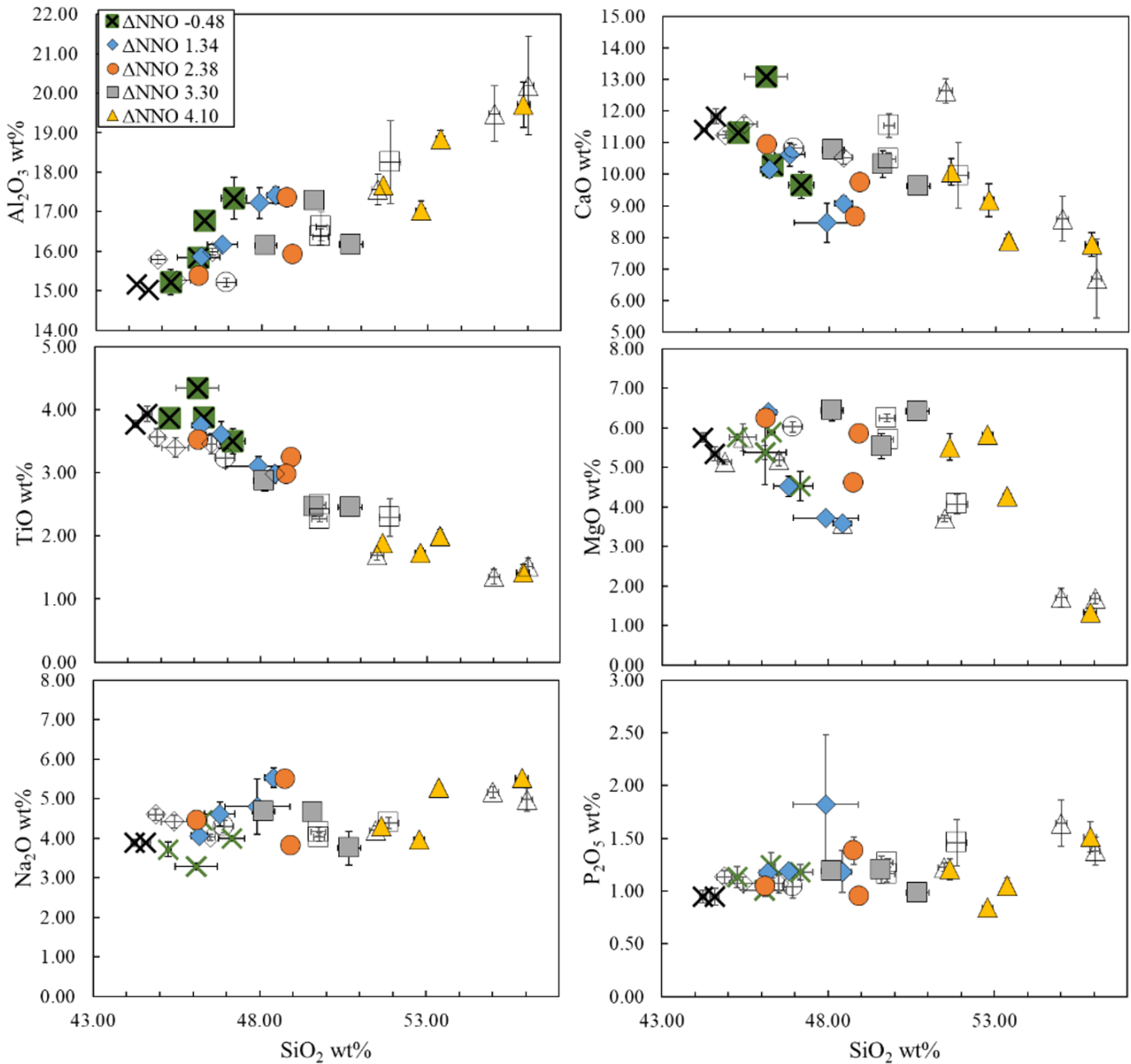


Fig. 2 Variation of oxides with SiO₂ of experimental glasses in S doped (coloured symbols) and FeS doped (open symbols) charges. When not shown, the error bars are smaller than the symbol size.

189 The major elements of glasses of both the S and FeS doped series (Table 3), show similar trends
 190 (Fig. 2). SiO₂ increases regularly with *f*O₂, from about 44 wt.% up to a of 56 wt.%, as does Al₂O₃,
 191 which reaches up to 20 wt.%, reflecting the absence of plagioclase crystallisation under the
 192 investigated conditions. Reflecting clinopyroxene crystallization, CaO shows the opposite

193 behaviour, decreasing with increasing SiO_2 and $f\text{O}_2$. The same trend is observed for TiO_2 and FeO .
 194 The alkalis show no clear trends, with the possible exception of Na_2O which increased slightly
 195 with SiO_2 . These fractionation trends reflect the effect of the main crystallising phases, but above
 196 all the increasing abundance of magnetite as $f\text{O}_2$ increases (Fig. 1).

197 The concentration of sulphur in the glasses does not differ between the S- or FeS-doped
 198 experiments (Fig.3). The charges produced at low $f\text{O}_2$ are significantly poorer in sulphur than those
 199 at high $f\text{O}_2$, the former having S concentration in the range 1000–2300 ppm, while the later have S

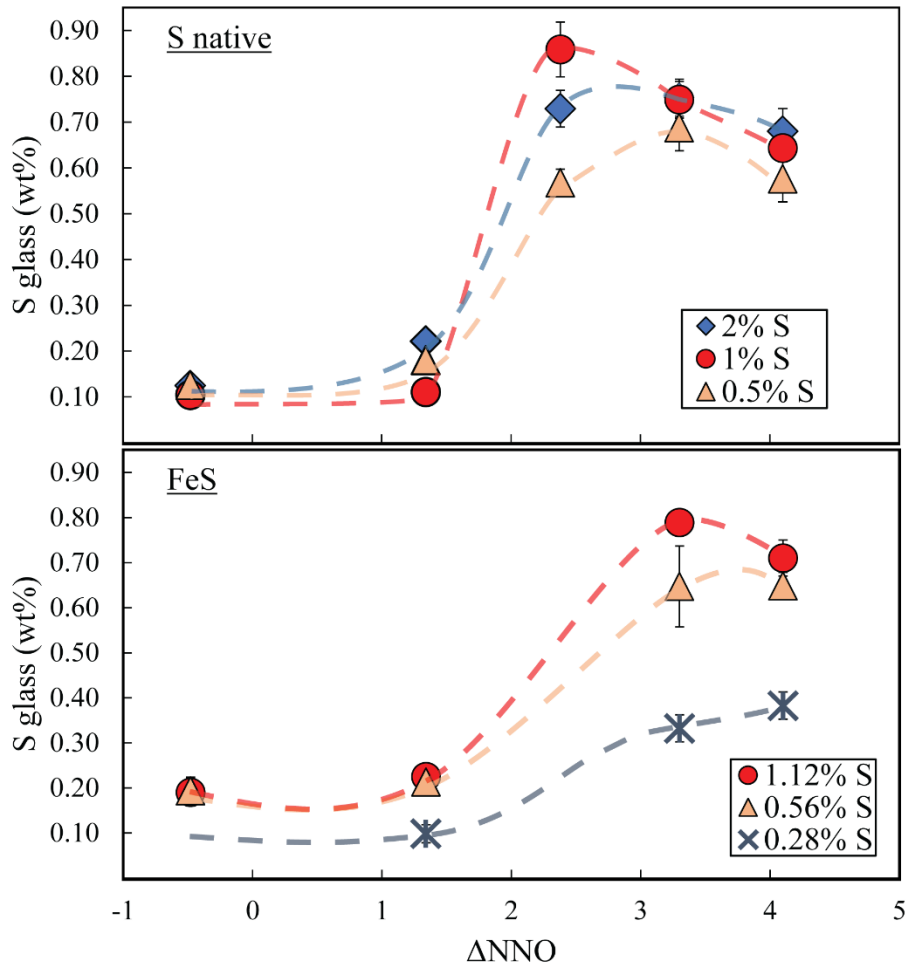


Fig. 3. Variation of S content of the glass with $f\text{O}_2$ as a function of wt.% of sulphur added to the capsules. When not shown, the error bars are smaller than the symbol size.

200 contents ranging between 3300–8800 ppm. Note however that the charge doped with 0.28 wt.% S
 201 using FeS yielded 0.8 wt.% dissolved S, which we attribute to an error in loading S to the charge.
 202 This individual run is not further considered.

203
 204 From inspection of the Mg# of the glass and of Fe-Mg minerals, the amount of sulphur added does
 205 not appreciably affect their composition at fixed $f\text{O}_2$, though under reduced conditions

206 (<NNO+1.5), charges with higher bulk S contents tend to have phases with higher Mg# (in
207 particular for charges with 2 wt.% added S). At high fO_2 the reverse is observed. Similarly, an
208 increase in fO_2 increases slightly the Mg# of the glass and olivine, as shown in figure in
209 Supplementary information (SIa). No clear trends with S appears for either amphibole or pyroxene
210 compositions (SIa).

211
212 The measured S contents in glasses saturated in pyrrhotite can be compared to those calculated
213 using the S-solubility model of Lesne et al. (2015), which was developed for hydrous alkali-rich
214 basalts, using the fS_2 determined by pyrrhotite (Table 2). We also calculated S contents using the
215 model of Boulliung and Wood (2023). The results are shown in Fig. 4, illustrating a general good
216 correspondence between calculated S contents with both models and those measured, though the
217 Boulliung and Wood (2023) model tends to underestimate S contents. Discrepancies likely reflect
218 analytical uncertainties in pyrrhotite composition as determined by EPMA, which translates into
219 an uncertainty in calculated fS_2 of order ± 1 log unit (e.g., Whitney, 1984). For instance, increasing
220 $\log fS_2$ of charge *lpm 29* from -1.02 to -0.5 (Table 2) would increase the calculated S content from

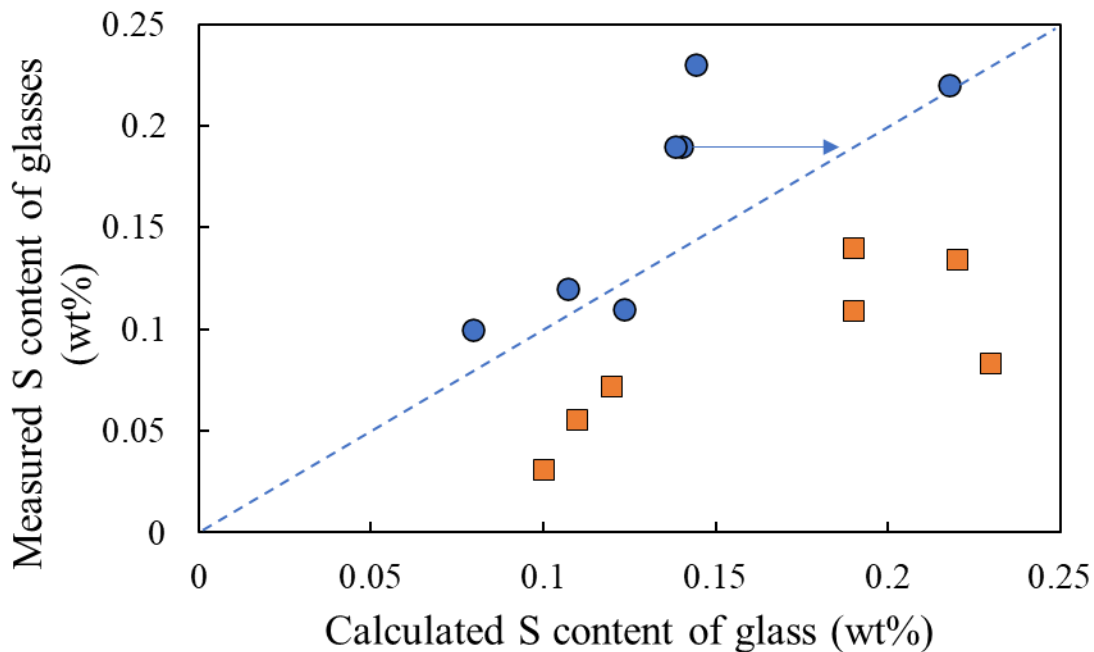


Fig. 4 Comparison between the measured S content of experimental glasses saturated in pyrrhotite with that calculated using the models of Lesne et al. (2015, blue symbols) and Boulliung and Wood (2023, orange symbols). The arrow shows the effect of increasing fS_2 by 0.5 log unit on the calculated S content of melt with the model of Lesne et al. (2015).

221 0.14 wt% to 0.19 wt%, the same as the measured amount (Fig. 4).

222

	ANNO	SiO ₂	TiO ₂	Al ₂ O ₃	FeO	MnO	MgO	CaO	Na ₂ O	K ₂ O	P ₂ O ₅	S	Total*
lpm 1	1.34	46.19 (0.25)	3.75 (0.10)	15.68 (0.14)	9.93 (0.36)	0.20 (0.08)	6.39 (0.10)	10.14 (0.25)	4.07 (0.05)	2.00 (0.20)	1.17 (0.06)	0.22 (0.02)	93.75
lpm 2		47.93 (0.98)	3.10 (0.15)	17.22 (0.39)	10.06 (0.19)	0.31 (0.07)	3.72 (0.15)	8.46 (0.62)	4.81 (0.62)	2.34 (0.700)	1.82 (0.66)	0.11 (0.01)	96.23
lpm 33		46.81 (0.45)	3.60 (0.21)	16.17 (0.07)	10.27 (0.34)	0.20 (0.07)	4.52 (0.25)	10.62 (0.37)	4.61 (0.25)	1.61 (0.25)	1.19 (0.06)	0.18 (0.01)	92.59
lpm 4		44.88 (0.22)	3.56 (0.14)	15.79 (0.11)	11.79 (0.12)	0.25 (0.05)	5.14 (0.10)	10.52 (0.15)	4.60 (0.15)	1.84 (0.06)	1.13 (0.06)	0.23 (0.01)	94.81
lpm 5		45.43 (0.40)	3.40 (0.16)	15.25 (0.21)	11.58 (0.28)	0.20 (0.09)	5.76 (0.57)	11.24 (0.72)	4.42 (0.16)	1.17 (0.34)	1.07 (0.06)	0.21 (0.03)	93.74
lpm 6		46.52 (0.15)	3.46 (0.16)	16.00 (0.09)	10.73 (0.34)	0.22 (0.08)	5.19 (0.27)	11.58 (0.16)	4.03 (0.08)	0.96 (0.14)	1.07 (0.09)	0.10 (0.02)	91.88
lpm 34		48.42 (0.27)	2.98 (0.11)	17.42 (0.21)	9.17 (0.30)	0.19 (0.05)	3.58 (0.09)	9.08 (0.22)	5.54 (0.25)	2.40 (0.10)	1.18 (0.02)	0.00 (0.01)	92.60
lpm 7	2.38	48.93 (0.23)	3.24 (0.06)	15.92 (0.12)	7.92 (0.09)	0.15 (0.03)	5.85 (0.06)	9.73 (0.13)	3.81 (0.06)	1.66 (0.09)	0.95 (0.08)	0.73 (0.04)	93.55
lpm 8		46.13 (0.28)	3.52 (0.14)	15.36 (0.10)	7.95 (0.26)	0.21 (0.02)	6.24 (0.17)	10.93 (0.23)	4.44 (0.09)	1.94 (0.17)	1.05 (0.09)	0.86 (0.06)	93.00
lpm 9		48.78 (0.15)	2.97 (0.10)	17.36 (0.21)	6.71 (0.21)	0.20 (0.07)	4.61 (0.18)	8.66 (0.22)	5.50 (0.07)	2.38 (0.14)	1.38 (0.13)	0.57 (0.03)	94.81
lpm 13	3.30	50.68 (0.35)	2.45 (0.11)	16.17 (0.22)	6.10 (0.30)	0.20 (0.08)	6.42 (0.09)	9.62 (0.14)	3.75 (0.42)	1.72 (0.06)	0.99 (0.05)	0.75 (0.04)	92.63
lpm 14		49.60 (0.21)	2.47 (0.16)	17.28 (0.22)	5.29 (0.19)	0.24 (0.09)	5.53 (0.32)	10.32 (0.42)	4.65 (0.12)	1.48 (0.13)	1.20 (0.12)	0.75 (0.04)	91.99
lpm 15		48.12 (0.33)	2.87 (0.16)	16.15 (0.10)	5.89 (0.20)	0.19 (0.07)	6.44 (0.26)	10.76 (0.14)	4.68 (0.07)	1.93 (0.18)	1.19 (0.06)	0.69 (0.05)	92.01
lpm- 16		49.77 (0.23)	2.27 (0.04)	16.37 (0.21)	6.07 (0.23)	0.12 (0.04)	6.25 (0.05)	10.48 (0.08)	4.17 (0.06)	1.72 (0.11)	1.16 (0.00)	0.79 (0.03)	91.16
lpm 17		49.79 (0.169)	2.49 (0.12)	16.62 (0.37)	5.83 (0.23)	0.20 (0.11)	5.17 (0.58)	11.54 (0.75)	4.03 (0.33)	1.14 (0.29)	1.27 (0.09)	0.65 (0.09)	89.92
lpm 18		51.87 (0.31)	2.29 (0.30)	18.26 (1.05)	5.17 (0.52)	0.26 (0.07)	4.07 (0.90)	9.96 (0.46)	4.39 (0.45)	1.58 (0.23)	1.46 (0.10)	0.33 (0.03)	89.41
lpm 19	4.10	52.79 (0.15)	1.73 (0.08)	17.04 (0.23)	5.24 (0.09)	0.17 (0.07)	5.83 (0.06)	9.19 (0.52)	3.97 (0.03)	3.97 (0.24)	1.80 (0.04)	0.85 (0.05)	91.44
lpm 20		51.66 (0.09)	1.89 (0.07)	17.67 (0.10)	4.74 (0.07)	0.22 (0.04)	5.52 (0.34)	10.07 (0.42)	4.32 (0.05)	1.37 (0.12)	1.21 (0.10)	0.64 (0.01)	90.53
lpm 21		55.88 (0.19)	1.42 (0.13)	19.71 (0.58)	3.35 (0.44)	0.23 (0.05)	1.33 (0.11)	7.77 (0.38)	5.52 (0.10)	2.01 (0.17)	1.51 (0.14)	0.58 (0.05)	91.59
lpm 22		51.50 (0.19)	1.69 (0.08)	17.57 (0.39)	5.13 (0.19)	0.25 (0.07)	3.71 (0.53)	12.64 (0.63)	4.20 (0.11)	0.65 (0.08)	1.22 (0.04)	0.71 (0.04)	90.99
lpmS 23		55.01 (0.17)	1.35 (0.11)	19.49 (0.71)	3.51 (0.52)	0.26 (0.10)	1.71 (0.95)	8.59 (0.81)	5.17 (0.14)	1.89 (0.24)	1.64 (0.22)	0.65 (0.03)	90.14
lpm S 24		56.03 (0.45)	1.52 (0.13)	20.19 (1.25)	3.74 (0.47)	0.20 (0.09)	1.68 (0.64)	6.69 (0.70)	4.98 (0.29)	2.76 (0.13)	1.38 (0.13)	0.38 (0.03)	89.50
lpmS 25		53.38 (0.12)	2.00 (0.11)	18.85 (0.21)	4.62 (0.22)	0.27 (0.11)	4.28 (0.05)	7.89 (0.07)	5.28 (0.11)	2.33 (0.10)	1.05 (0.08)	0.01 (0.01)	91.49
lpm 26	-0.48	46.28 (0.12)	3.88 (0.06)	16.78 (0.22)	8.89 (0.11)	0.22 (0.09)	5.88 (0.06)	10.28 (0.06)	4.45 (0.05)	1.77 (0.10)	1.24 (0.12)	0.12 (0.01)	92.87
lpm 27		47.16 (0.38)	3.50 (0.20)	17.35 (0.52)	10.19 (0.36)	0.24 (0.14)	4.53 (0.37)	9.66 (0.49)	4.00 (0.77)	1.99 (0.06)	1.18 (0.07)	0.10 (0.01)	94.19
lpm 28		45.26 (0.07)	3.86 (0.15)	15.22 (0.32)	11.65 (0.26)	0.21 (0.05)	5.77 (0.07)	11.31 (0.17)	3.72 (0.19)	1.57 (0.06)	1.13 (0.10)	0.13 (0.01)	93.35
lpm 29		44.24 (0.10)	3.77 (0.06)	15.16 (0.06)	12.64 (0.18)	0.21 (0.04)	5.75 (0.23)	11.40 (0.27)	3.89 (0.09)	1.55 (0.25)	0.94 (0.06)	0.19 (0.03)	92.82
lpm 30		44.59 (0.14)	3.93 (0.12)	15.02 (0.23)	12.36 (0.26)	0.20 (0.05)	5.34 (0.14)	11.83 (0.23)	3.89 (0.09)	1.42 (0.11)	0.95 (0.08)	0.19 (0.03)	93.35
lpm 32		46.09 (0.64)	4.34 (0.15)	15.85 (0.14)	9.92 (0.75)	0.14 (0.05)	5.38 (0.81)	13.09 (1.24)	3.29 (0.17)	0.79 (0.18)	1.01 (0.06)	0.01 (0.01)	92.35

223

Table 3 Major elements compositions, normalized to 100% anhydrous, and S contents of quenched glasses; *Original total.

224

225 *4.2 Mass balance and ImageJ*

226 For most experiments, the volumetric percentage of glass obtained by mass balance is similar to
227 that calculated using ImageJ (Table 4). The mass balance estimates indicate that amphibole content
228 peaks at 40 wt.%, while clinopyroxene abundance is generally below 10 wt% and not higher than
229 19 wt% (Table 4). Similarly, olivine proportion does not exceed 10 wt.%. The fact that amphibole
230 proportion is higher than that in the rocks (<5 wt%, e.g. Ubide et al., 2023) reflects the lower
231 temperature of our experiments.

232 The calculated wt.% of glass correlates well with P₂O₅ abundance, as P is incorporated only by
233 apatite (SIb). The dashed line in SIb is calculated assuming perfectly incompatible behaviour of
234 P₂O₅. Deviations from it signify apatite formation, which occurs after 20–30 wt.% crystallisation.

235

236

	Mass balance										ImageJ estimation		
	Gl wt%	Ol wt%	Amph wt%	Cpx wt%	Fes wt%	Anhy wt%	Mt wt%	Ilm wt%	Ap wt%	Gl vol%	Sr	Gl %	
lpm 1	75.6 (0.02)	<1 (0.01)	18.5 (0.03)	4.6 (0.01)	2.8 (0.002)	-	-	-	-	-	79.4	0.22	86.5
lpm 2	56.0 (0.01)	<1 (0.03)	33.4 (0.03)	8.2 (0.01)	1.1 (0.01)	-	1.7 (0.01)	-	-	-	61.0	0.18	55.1
lpm 33	75.1 (0.03)	3.6 (0.01)	15.9 (0.04)	3.0 (0.01)	-	-	2.4 (0.003)	-	-	-	79.1	0.41	72.2
lpm 4	78.6 (0.03)	3.6 (0.01)	10.0 (0.04)	4.4 (0.02)	1.3 (0.005)	-	1.9 (0.01)	-	-	-	82.6	0.02	84.3
lpm 5	86.6 (0.03)	2.5 (0.01)	7.8 (0.03)	0.2 (0.03)	-	-	2.9 (0.003)	-	-	-	89.5	0.53	72.2
lpm 6	77.7 (0.02)	4.8 (0.01)	15.8 (0.03)	<1 (0.01)	-	-	2.5 (0.003)	-	-	-	81.4	1.22	77.4
lpm 34	62.3 (0.02)	2.5 (0.004)	17.0 (0.03)	14.0 (0.01)	-	-	4.3 (0.003)	-	-	-	68.0	0.16	57.0
lpm 7	90.1 (0.01)	3.3 (0.002)	-	-	-	-	5.5 (0.003)	1.1 (0.002)	-	-	93.7	7.22	95.2
lpm 8	87.4 (0.01)	1.5 (0.003)	-	5.1 (0.009)	-	-	6.0 (0.002)	-	-	-	92.4	1.20	99.3
lpm 9	54.7 (0.03)	<1 (0.01)	26.1 (0.05)	11.8 (0.02)	-	-	8.5 (0.003)	-	-	-	77.9	0.08	68.2
lpm 13	89.9 (0.01)	1.8 (0.003)	-	-	-	-	12.2 (0.004)	<1 (0.003)	-	-	95.3	9.99	91.8
lpm 14	76.7 (0.01)	2.1 (0.003)	-	12.7 (0.01)	-	-	8.5 (0.002)	-	-	-	84.6	6.15	78.7
lpm 15	80.0 (0.01)	-	-	11.6 (0.01)	-	-	8.3 (0.002)	-	-	-	85.8	1.59	70.6
lpm 16	77.2 (0.01)	-	-	9.8 (0.01)	-	-	13.4 (0.003)	<1 (0.003)	-	-	84.5	0.80	84.5
lpm 17	79.9 (0.01)	2.1 (0.003)	-	4.3 (0.01)	-	-	7.0 (0.003)	-	-	-	86.8	1.54	84.6
lpm 18	51.5 (0.01)	-	37.1 (0.03)	1.6 (0.02)	-	-	9.8 (0.003)	-	-	-	60.8	3.10	72.3
lpm 19	89.5 (0.01)	7.4 (0.01)	-	<1 (0.02)	-	5.7 (0.004)	11.4 (0.003)	0.4 (0.003)	-	-	94.0	0.40	93.4
lpm 20	56.8 (0.02)	<1 (0.01)	33.3 (0.04)	3.6 (0.01)	-	-	12.1 (0.004)	<1 (0.003)	-	-	63.4	1.07	68.5
lpm 21	43.0 (0.01)	-	39.7 (0.02)	9.0 (0.01)	-	-	8.4 (0.002)	-	-	-	48.57	0.96	59.8
lpm 22	77.8 (0.01)	6.1 (0.003)	-	2.5 (0.01)	-	-	13.6 (0.002)	-	-	-	86.6	4.48	84.7
lpm 23	47.6 (0.01)	-	27.9 (0.01)	13.8 (0.01)	-	-	10.7 (0.002)	-	-	-	57.5	2.51	62.8
lpm 24	45.1 (0.01)	-	31.1 (0.03)	12.0 (0.04)	-	-	10.3 (0.002)	-	1.6 (0.004)	-	51.7	0.97	55.6
lpm 25	57.3 (0.01)	-	14.4 (0.01)	18.8 (0.01)	-	-	9.5 (0.002)	-	-	-	67.2	1.27	66.4
lpm 26	77.1 (0.0)	0.8 (0.01)	8.4 (0.04)	9.6 (0.01)	4.1 (0.002)	-	-	-	-	-	81.5	0.26	72.3
lpm 27	67.0 (0.02)	3.2 (0.004)	18.8* (0.04)	<1 (0.02)	2.1 (0.002)	-	-	-	-	-	71.7	1.22	82.5
lpm 28	99.0 (0.13)	<1 (0.01)	<1 (0.14)	-	-	-	<1 (0.003)	-	-	-	99.0	1.19	94.8
lpm 29	93.1 (0.01)	4.8 (0.003)	-	<1 (0.01)	1 (0.003)	-	-	-	-	-	95.0	0.20	89.5
lpm 30	96.6 (0.03)	6.6 (0.003)	-	<1 (0.01)	0.2 (0.003)	-	0.5 (0.01)	-	-	-	97.5	0.53	86.5
lpm 32	80.0 (0.12)	9.3 (0.005)	17.5* (0.13)	<1 (0.01)	-	-	1.7 (0.01)	-	-	-	83.1	2.96	97.8

238 Table 4. Phase proportions calculated by mass balance and image analyses (glass, using ImageJ software).

239 *Amphibole partly of inferred quench origin.

241 **5. Discussion**

242 Our experiments emphasise the control of fO_2 on the S-carrying capacity of silicate melts, as shown
 243 in many previous studies (e.g., Carroll and Rutherford, 1985; Luhr, 1990; Scaillet et al., 1998; Jugo
 244 et al., 2005). The effects of sulphur on phase relations are subtle and complex, depending on the
 245 fO_2 of the experiments. In particular, amphibole is unstable at intermediate fO_2 , between $NNO+2.38$
 246 and $NNO+4.10$, and S-rich conditions, while sulphide precipitates only below $NNO+1.5$. The
 247 minor differences noted between the S- and FeS-doped series may be explained by the presence of
 248 higher iron abundance in the latter case. Sulphur does not appear to affect significantly the
 249 composition of individual phases, except for a tendency of FeMg silicate phases to become more
 250 Mg-rich with S addition. In contrast, oxygen fugacity does affect phase compositions, in particular
 251 olivine and glass, whose Mg# increases markedly under more oxidising conditions in both the S-
 252 doped and FeS-doped experiments.

253 The mass balance data also show no systematic effect of sulphur on phase proportions in the
 254 different experiments, aside from the obvious cases of sulphide or anhydrite. Here again, oxygen
 255 fugacity appears to exert the stronger influence. As expected, the amounts of oxides, both
 256 titanomagnetite and ilmenite, increase from reducing to oxidising conditions (Table 4). In detail,

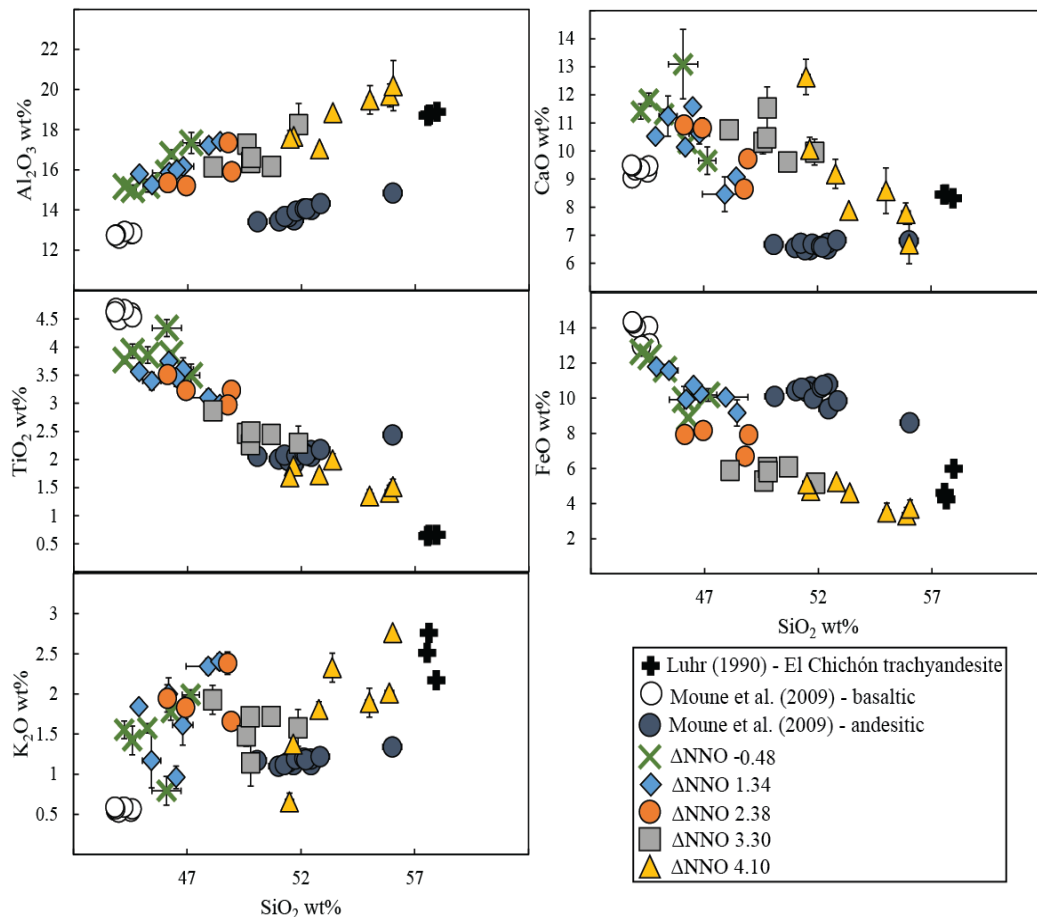


Fig. 5 Concentration of major element versus SiO_2 wt%. The experiments are compared to the water-saturated, $1050^\circ C$ and 200-300 MPa experiments of Moune et al. (2009) and the composition A (trachyandesite) performed at $1000^\circ C$, 200 MPa from Luhr (1990).

257 amphibole abundance increases slightly in more oxidised runs than in reduced ones, but with no
258 clear difference between sulphur-rich and sulphur-poor charges. This confirms that oxygen
259 fugacity, not the amount of sulphur in the system, exerts the stronger control on phase proportions.

260 From the perspective of sulfur content in the residual glass, both sets of experiments show a
261 consistent pattern of increasing sulfur content with elevated fO_2 . The changes in melt composition
262 resulting from fO_2 variation are perhaps best illustrated by changes in Ti and Fe contents: from
263 NNO-0.48 to NNO+4.10, both the TiO_2 and FeO abundances in the glass decrease by 75 wt%,
264 reflecting substantial crystallisation of Fe-Ti oxides. This increase in crystallisation is accompanied
265 by an increase in abundances of Al_2O_3 and SiO_2 in the glass, owing to the lack of plagioclase
266 crystallisation. These significant changes in melt composition do not, however, seem to affect the
267 overall positive effect that fO_2 has on S concentrations.

268 Our results can be compared with sulphur solubility experiments performed at comparable P-T-
269 H_2O conditions on hydrous basaltic-andesitic magmas erupted in contrasting geodynamic contexts:
270 i) at Hekla volcano in 2000, which is taken to here represent mid-ocean ridge volcanism, though
271 interaction with plume material is possible (Moune et al., 2009); ii) the trachyandesite magma
272 erupted at El Chichón volcano in 1982, which belongs to an arc setting (Luhr, 1990) though some
273 rift related processes are likely (Arce et al., 2014). The water-saturated, 1050°C and 200–300 MPa
274 experiments of Moune et al., (2009), and the composition A (trachyandesite) performed at 1000°C,
275 200 MPa from Luhr (1990), are compared with our data in Fig. 5. At any given SiO_2 , differences
276 in some oxide contents (e.g., CaO, Al_2O_3) are evident. These can be attributed to bulk
277 compositional effects (Fig. 5) and to slightly different experimental conditions which impart
278 different degrees of crystallization. The broad correspondences remain when oxygen fugacity is
279 considered (Figure S1c). The TiO_2 content of the andesitic charges of Moune et al (2009) and Luhr
280 (1990) are lower than ours, reflecting the lower Ti content of the corresponding starting materials.
281 This is particularly evident in the Luhr (1990) experiments, in which the concentration of TiO_2 in
282 the starting composition is so low that no difference exists between reduced and oxidised
283 conditions. Based on these data, it appears that the presence of sulphur does not significantly affect
284 the concentrations of the major elements of residual melts. Irrespective of geodynamic context, the
285 factor that most influences melt composition is oxygen fugacity.

286 As in many previous studies(e.g., Carroll and Rutherford, 1985; Liu et al., 2007; Moune et al.,
287 2009), our experiments reveal a significant difference in the amount of sulphur in the glasses
288 between low and high fO_2 experiments (Fig. 6). At low fO_2 , the sulphur concentrations in the
289 glasses measured by Moune et al (2009) and Luhr (1990) are comparable to those found in our
290 experiments, most falling in the interval 1000–2500 ppm. Furthermore, as noted by Moune et al.
291 (2009), at fO_2 between NNO-0.48 and NNO1.34, sulphur abundance in the glass increases in
292 proportion to the increase of added sulphur, until bulk S exceeds 0.5 wt.% (Fig 6). Thereafter, the
293 S content in the glass levels off at 2000 ± 100 ppm. At fO_2 above NNO+2.38, a similar pattern is
294 observed with a positive trend up to about 1 wt.% sulphur added, at which point the dissolved S
295 levels off at 0.7 wt%.

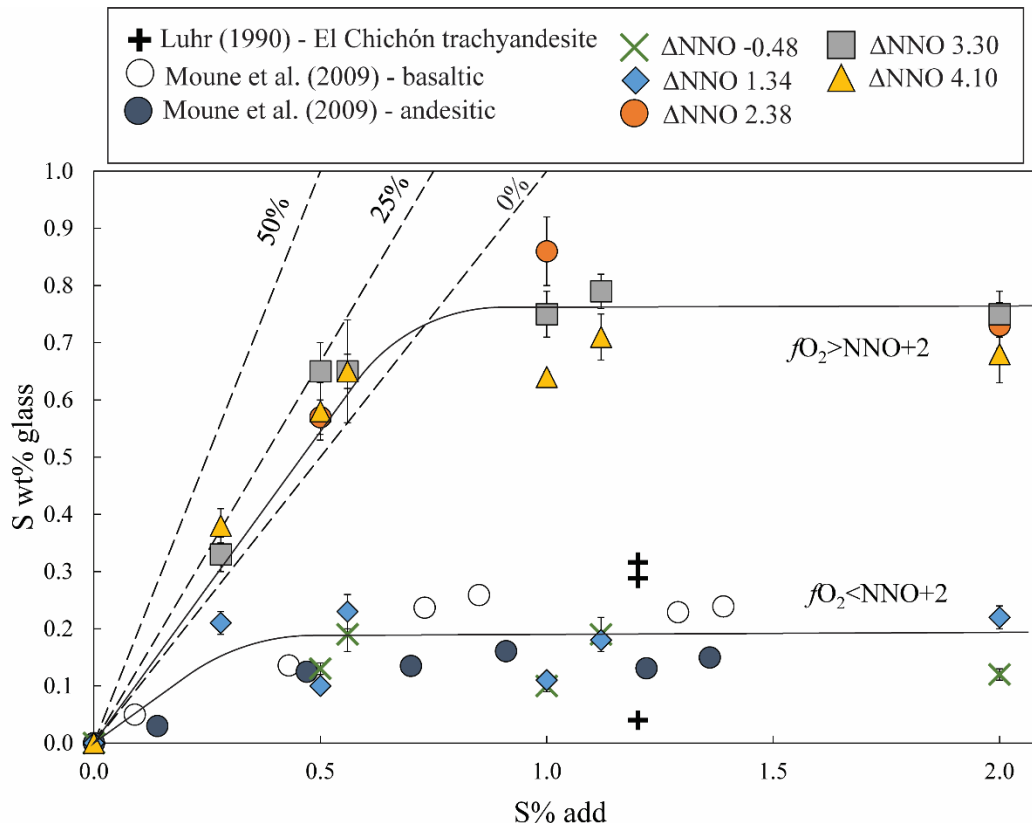


Fig.6 Sulphur concentration in the melt versus the amount of sulphur added in the runs. The experiments are compared to the water-saturated, 1050°C and 200-300 MPa experiments of Moune et al. (2009) and the composition A (trachyandesite) performed at 1000°C, 200 MPa from Luhr (1990). The dashed trendlines are calculated assuming an incompatible behaviour of S at 50%, 25% and 0% of crystallization.

296 The experiments of Luhr (1990) carried out under oxidised conditions resulted in lower S
 297 concentrations in the glass than we obtained for the same amount of sulphur added. Anhydrite
 298 crystallization in the Luhr (1990) runs, which did not occur in our experiments under the same
 299 conditions, likely explains this. The levelling off of both trends at high bulk S contents likely results
 300 from the buffering effect of other S-bearing phases. In addition to fluid, under reducing conditions
 301 this would be sulphide, while under oxidising conditions this would be anhydrite. Oxidised charges
 302 with less than 0.5 wt.% added S fall on, or close to, the 1-to-1 correlation line, which shows that
 303 under these conditions a significant proportion of S resides in the melt phase (those data that fall
 304 above the 1/1 line reflect the amount of crystallisation of charges).

305

306

307

308 5.1 Significance for understanding the La Palma 2021 eruption

309 The pre-eruptive fO_2 of Cumbre Vieja 2021 basanite has been broadly constrained from V
 310 systematics in olivine to fall between NNO+0.6 and NNO+1.3 (Day et al., 2022). We note however
 311 that a recent reassessment of V behaviour has concluded that current formulations of this
 312 oxybarometer tend to overestimate fO_2 by up to 0.7 log unit in hydrous basalts (Erdmann et al.,
 313 2024), which would bring the La Palma magma redox state into the NNO-NNO+1 range.

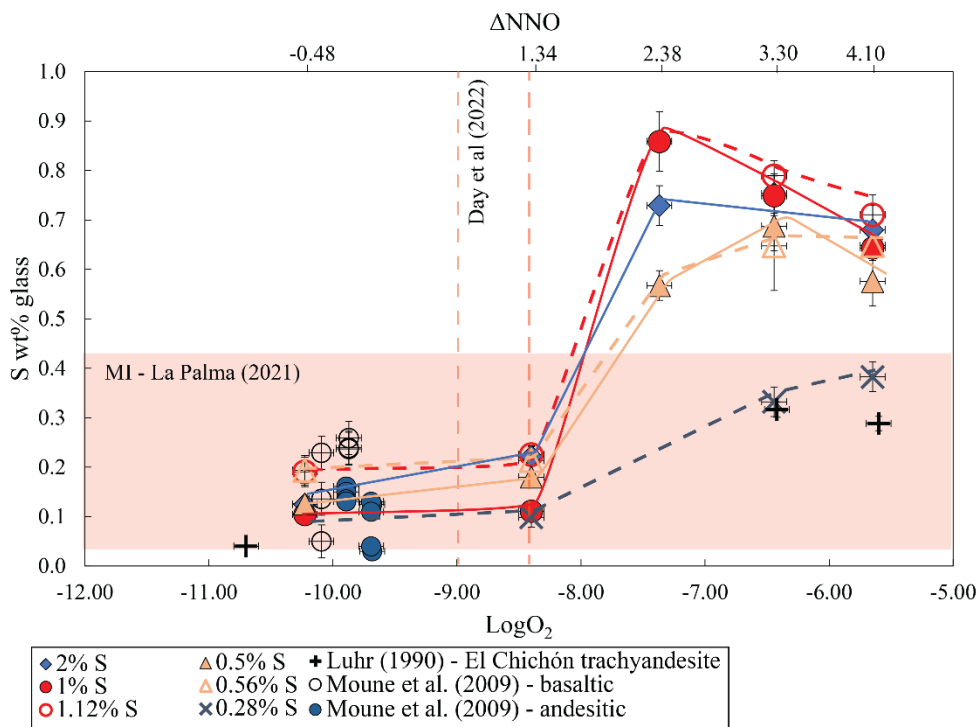


Fig. 7 Sulphur concentration in the melt versus $\log fO_2$. The experiments are compared to the water-saturated, 1050°C and 200-300 MPa experiments of Moune et al., 2009 and the composition A (Trachyandesite) performed at 1000°C, 200 MPa from Luhr, 1990; MI-La Palma (2021) = S wt% in melt inclusions (Castro and Feisel, 2022; Burton et al., 2023; Dayton et al., 2024).

314 Considering a NNO-NNO+1.3 range, our data indicate that under these conditions the bulk magma
 315 S content was ~2500–5000 ppm, a significant part of which was dissolved in the melt, broadly
 316 consistent with melt inclusion analyses (Fig.7) (e.g., Castro and Feisel, 2022; Burton et al., 2023;
 317 Dayton et al., 2024). Note that the highest S content so far measured in melt inclusions (4800 ppm,
 318 Burton et al., 2023) points to fO_2 at the upper end of the range inferred from V in olivine (Fig. 10),
 319 or higher temperatures. The occasional occurrence of sulphides (as inclusions in phenocrysts) in
 320 erupted products (Andujar et al., submitted) is consistent with our experiments at NNO+1.34,
 321 although the absence of sulphide in the matrix glass suggests that the erupting magma was not
 322 saturated in sulphide.

323 Our experiments show that to achieve the observed S content analysed in melt inclusions of La
 324 Palma 2021 basanite (around 3000 ppm S) at the inferred pre-eruptive fO_2 between NNO+0.6 and
 325 NNO+1.6 (Day et al., 2022), the fS_2 should be around 0.1–1 MPa, as recorded by the composition
 326 of pyrrhotite in our run products (Table 2).

327 Using these constraints, in what follows we have have carried out calculations aimed at modelling
328 the fluid phase composition for three different scenarios: (1) we have first calculated the fluid
329 composition at equilibrium with the basanite magma lying in the crustal reservoir, which is inferred
330 to lie at ~ 300 MPa, based on seismic source locations and petrological arguments (e.g., D’Auria
331 et al., 2022; Del Fresno et al., 2023b; Ubide et al., 2023; Dayton et al., 2024; Andujar et al.,
332 submitted). (2) We next perform calculations of magma degassing during uprise, starting at 300
333 MPa with variable amount of exsolved fluid. (3) Finally, we simulate degassing from higher
334 pressures (i.e. deeper levels) and higher temperature (about 1125°C), in keeping with the elevated
335 CO₂ dissolved contents (up to 1.2 wt%) retrieved from olivine inclusions (e.g., Zanon et al., 2023;
336 Dayton et al., 2024) and seismic data (e.g., D’Auria et al., 2022; Del Fresno et al., 2023) which
337 point to a mantle source at 400-800 MPa.

338 (1) For the first step, we use the following constraints: a pre-eruptive dissolved CO₂ content
339 ranging from 3000–5000 ppm, and a dissolved H₂O_{melt} of 1–3 wt%, drawing on melt
340 inclusion analyses (e.g., Burton et al., 2023; Dayton et al., 2023). We perform calculations
341 at 1080°C, which corresponds to the inferred temperature for the basaltic magma at
342 equilibrium with amphibole ((González-García et al., 2023)González-García et al., 2023;
343 Sandoval-Velasquez et al., 2023; Andujar et al., submitted), using an MRK equation of state
344 for fluid coupled to the S solubility model of Lesne et al. (2015), calibrated for alkali-rich

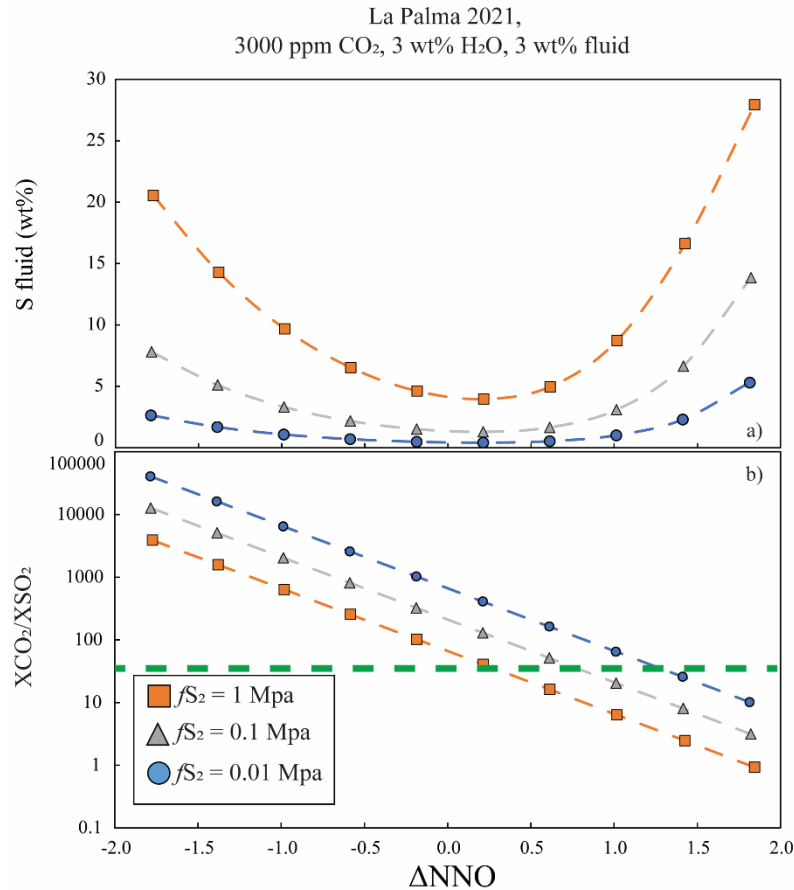


Fig. 8 (a) Evolution of the S content of the excess fluid in the reservoir at 300 MPa with fO_2 . (b) Evolution of the ratio $X\text{CO}_2/X\text{SO}_2$ of the fluid with ΔNNO . The calculations have been made at three different fS_2 ; The thick green line shows the $X\text{CO}_2/X\text{SO}_2$ ratio of volcanic gases measured at la Palma during explosive emissions (Burton et al., 2023). See text for details.

345 basalt melts, and to the CO₂-H₂O solubility model of Jímenez-Mejías et al. (2021),
 346 calibrated for a basanite from the Canary islands. The calculation then yields the saturation
 347 pressure in H₂O, CO₂, SO₂ and H₂S fluid species. The key assumption is that of equilibrium
 348 between the fugacities of volatiles in the fluid with those in the melt (e.g., Lesne et al.,
 349 2015). Given uncertainty in the magma redox state, and in its possible variation during
 350 decompression (e.g., Burgisser and Scaillet, 2007; Moussallam et al., 2016), we performed
 351 the calculations for a range of fO_2 between NNO-2 and NNO+2. Fig 8a shows the variation
 352 of S content of the fluid in the reservoir at 300 MPa with fO_2 , calculated for three different
 353 fS_2 . This calculation gives the composition of fluids at the surface if they could leave the
 354 crustal reservoir on their own, i.e. without being accompanied by melts, and traversing the
 355 crustal section unmodified. Although this scenario is possibly not directly applicable to the
 356 La Palma 2021 eruption, it provides context for the interpretation of gas monitoring during
 357 repose periods. In the range of fO_2 inferred by Day et al. (2022), the S content of the fluid
 358 falls between 1 and 10 wt%, depending on fS_2 , comparable with S contents calculated for
 359 more silicic compositions (e.g., Scaillet et al., 2003) and to that calculated by mass balance

360 for most of our experiments (Table 2). The calculations further show that X_{CO_2}/X_{SO_2}
 361 progressively decreases as f_{O_2} increases (Fig. 8b). In the f_{O_2} interval NNO+0.7 to
 362 NNO+1.3, X_{CO_2}/X_{SO_2} ranges from ~ 2 up to ~ 100 , within the range of measurements of
 363 volcanic gas emissions during the 2021 La Palma eruption (Burton et al., 2023). Measured
 364 ratios range from to 35 for explosive activity down to less than 10 for effusive emissions
 365 (Burton et al., 2023), and the higher end is to be favoured as a characteristic of gas-rich
 366 magma, presumably of deeper provenance.

367 (2) We next consider degassing during magma ascent, especially of S and H₂O, which can
 368 exsolve and separate from the melt extensively near the surface (Oppenheimer et al., 2014).
 369 The full calculation should also take into account the possible role of an excess fluid in the
 370 crustal reservoir. For instance, the bulk CO₂ content of La Palma magma has been estimated
 371 to be at 4 ± 1.5 wt% based on the measured S emissions and the average X_{CO_2}/X_{SO_2} ratio
 372 (Burton et al., 2023). Taking a conservative value of 3 wt% fluid (with 3 wt% H₂O and

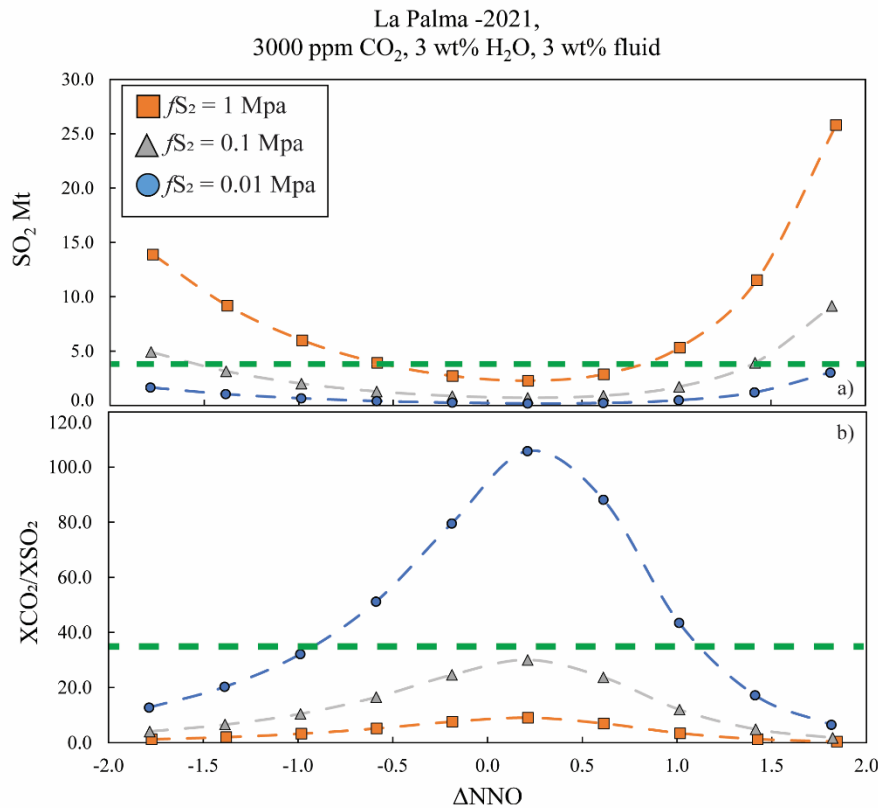


Fig. 9 (a) Evolution of total amount of SO_2 degassed by 0.2 km^3 of basanite magma with f_{O_2} expressed as ΔNNO . (b) Evolution of the X_{CO_2}/X_{SO_2} ratio of the gas emitted at the vent with ΔNNO . The calculations have been performed at 1080°C .

373 3000 ppm CO₂ dissolved in melt, which correspond to the volatile contents of a fluid
 374 saturated basanite at 300 MPa), we calculate as a function of oxygen fugacity both the total

375 amount of S released by the 0.2 km³ of erupted magma, and the XCO₂/XSO₂ ratio of the
376 gas at the vent (i.e. melt+fluid), accounting for the 400– 600 ppm of S that remains in matrix
377 glass (Fig. 12). With these constraints and assuming an *f*O₂ of ~ NNO+1, 2-4 Mt SO₂, we
378 find that the pre-eruptive magma must have had an *f*S₂ in the range 0.1-1 MPa (Fig. 9a). A
379 *f*S₂ significantly lower than 0.1 MPa will fall short in reproducing this figure. With respect
380 to the final XCO₂/XSO₂ ratio (i.e. the one measured at the vent), the same set of calculations
381 shows that such a ratio displays a bell-shaped pattern, with a maximum in between NNO
382 and NNO+0.5 (fig.9b). For *f*S₂ values in the range 0.1-1 MPa, the maximum possible
383 XCO₂/XSO₂ ratio is about 30, lying slightly above NNO, i.e. at an *f*O₂ more reduced than
384 that retrieved from V systematic.

385 It is also interesting to consider the X_{H_2O}/X_{SO_2} ratio, which was also measured during La Palma
 386 2021 eruption (Burton et al., 2023). The variation of this ratio with fO_2 (as for X_{CO_2}/X_{SO_2}) with
 387 the amount of excess fluid in the reservoir is shown in Fig. 10b. Here the calculations are made for
 388 a magma at 300 MPa with 4000 ppm CO_2 , 2 wt% H_2O and for $fS_2=0.2$ MPa, at $1080^\circ C$, also
 389 consistent with available melt inclusion and phase equilibrium constraints for the top portion of the
 390 plumbing system (González-García et al., 2023; Sandoval-Velasquez et al., 2023; Andujar et al.,
 391 submitted). As with the previous calculations, both ratios exhibit a similar bell shaped trend with
 392 fO_2 . They are both sensitive to the amount of free fluid: as it increases, so the X_{H_2O}/X_{SO_2} ratio
 393 drops, while the X_{CO_2}/X_{SO_2} increases, due to the contrasting H_2O and CO_2 contents in melt and
 394 fluid phases. Gas emissions during the most explosive phase of La Palma eruption had an

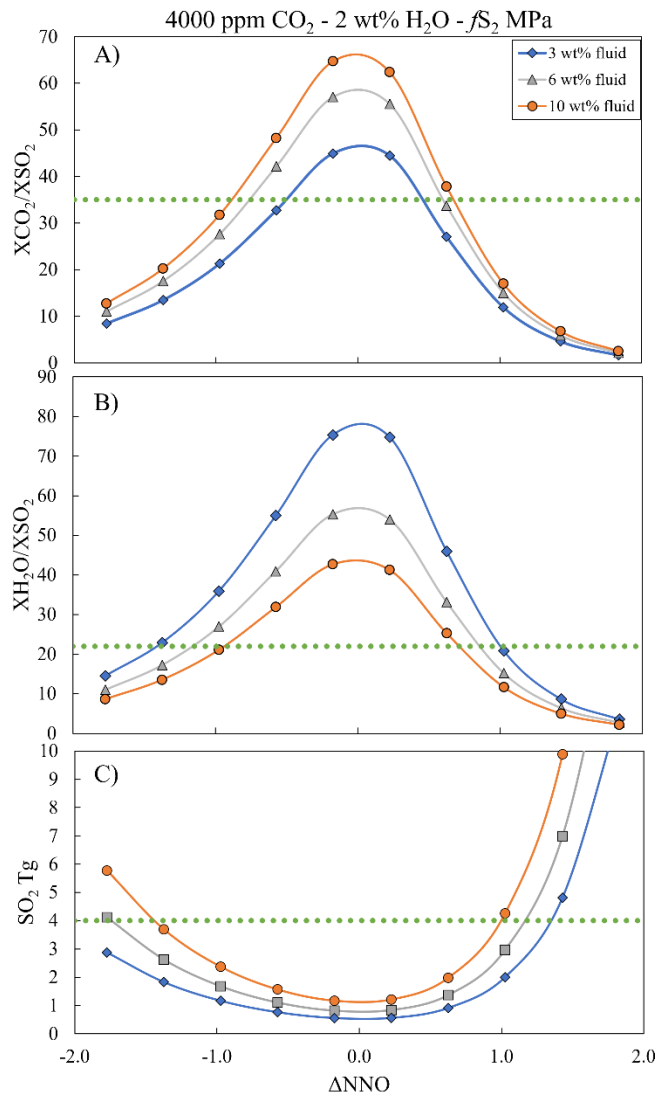


Fig. 10. Evolution of the X_{H_2O}/X_{SO_2} (a) and X_{CO_2}/X_{SO_2} (b) ratios of gases vented at 0.1 MPa with fO_2 , for different amounts of exsolved fluid in the reservoir at 300 MPa. (c) Evolution of the mass of SO_2 produced for the three different amounts of fluid. In all panels the thick horizontal green dashed line indicates the measured value of the corresponding parameter.

395 X_{CO_2}/X_{SO_2} of ~ 35 and an X_{H_2O}/X_{SO_2} ratio of ~ 22 (Burton et al., 2023). For the conditions
 396 shown in Fig. 10, these ratios are reproduced at around NNO+0.5 to NNO+1 for 6 wt% excess
 397 fluid, broadly consistent with previous inferences. Clearly, the amount of SO_2 released increases
 398 with the amount of pre-eruptive fluid in the crustal reservoir (Fig. 13c). For this set of conditions,
 399 fO_2 in the range NNO+1 to NNO+1.5 are required to yield 4 Tg SO_2 . These calculations point
 400 therefore to the presence of a significant amount of free fluid in the plumbing system, as indicated
 401 by previous work (e.g., Burton et al., 2023; Sandoval-Velasquez et al., 2023; Zanon et al., 2024)).

402 (3) The last set of calculations explores the deeper part of the plumbing system. As noted
 403 earlier, melt inclusions hosted by olivine record a range of dissolved CO_2 , up to 5000 ppm
 404 (e.g., Dayton et al., 2024). If account is made for the occurrence of exsolved fluid in the

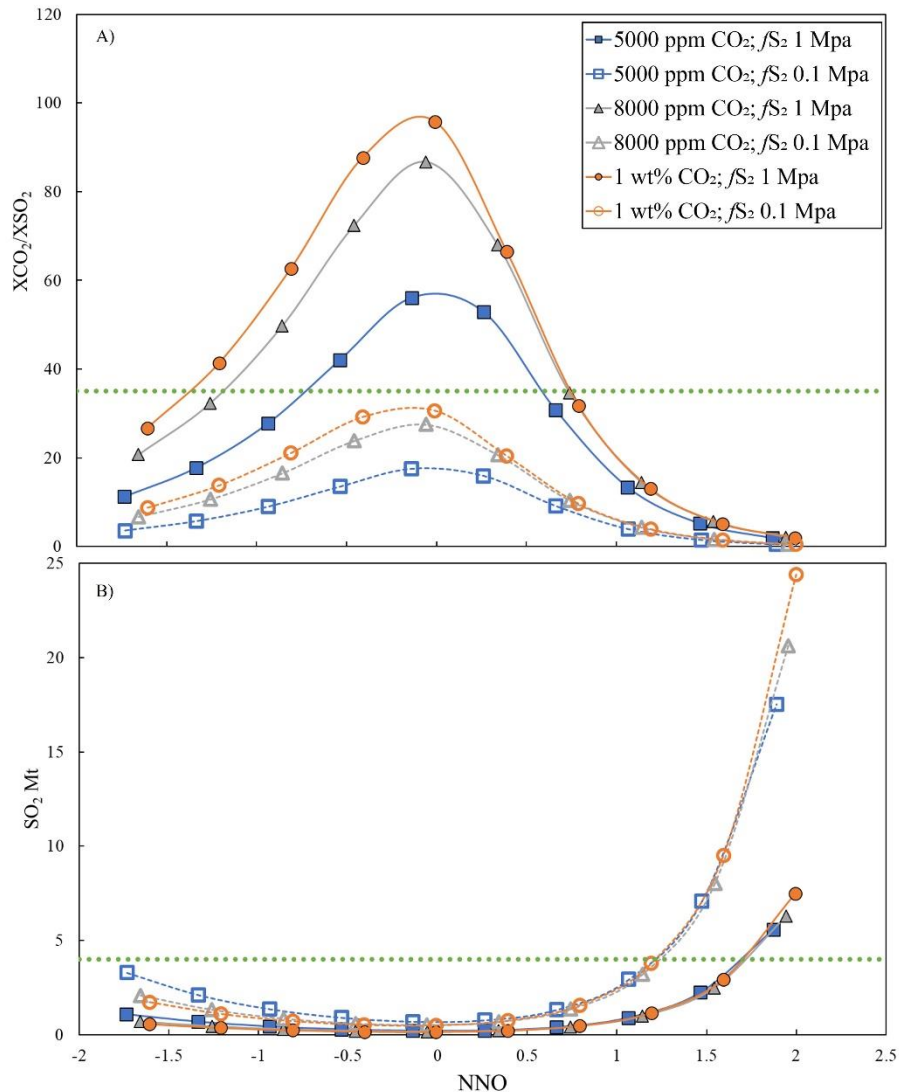


Fig. 11(a) Evolution of total amount of SO_2 degassed by 0.2 km^3 of basaltic magma with fO_2 expressed as ΔNNO with increasing CO_2 from 5000 ppm to 10000 ppm. (b) Evolution of the X_{CO_2}/X_{SO_2} ratio of the gas emitted at the vent with ΔNNO with increasing CO_2 from 5000 ppm to 10000 ppm. The calculations have been performed at 1125°C . In all panels the measured values of the corresponding parameter are in green dashed line (burton et al., 2023).

405 melt inclusions, the CO₂ content rises up to 1.2 wt% (Dayton et al., 2024), underscoring the
406 deep mantle provenance of some of the magma erupted during the eruption. We have
407 therefore also carried out calculations using higher dissolved CO₂, from 5000 to 10000 ppm
408 (corresponding to pressures in the range 400-800 MPa). We keep the excess fluid at 3 wt%
409 as in most calculations above and the amount of H₂O dissolved at 3 wt% (hence the total
410 amount of volatiles sums up to over 6 wt%). Results are shown on figure 11. In terms of
411 XCO₂/XSO₂, increasing pressure makes high fS_2 (1 MPa) less likely than a moderate one
412 (0.1 MPa), since the family of curves corresponding to $fS_2=1\text{MPa}$ does not allow to
413 reproduce the observed XCO₂/XSO₂ ratio of vented gases. Note that for an $fS_2=0.1\text{ MPa}$,
414 the intersection happens at around NNO+1, which is an fO_2 slightly lower than the one
415 inferred by Day et al. (2022).

416

417 For what regards the amount of SO₂ released, a magma with an fS_2 of 1 MPa would require an
418 fO_2 slightly over NNO, while that with an fS_2 of 0.1 MPa would require slightly more oxidizing
419 conditions, both fS_2 being compatible with the inferred range of redox state of La Palma magma
420 (Day et al., 2022).

421 The above sets of calculations show that reproducing the observations reported for La Palma
422 eruption, in particular the S content of melt inclusions, the gas composition, and the amount of S
423 released, requires a subtle combination of fO_2 , fS_2 and amount of fluid of the magma (in addition
424 to T and P). Elevated S contents in the melt point to fO_2 conditions above NNO (Fig.6). The fS_2
425 should be in the vicinity of 0.1 MPa in order to reproduce the amount of SO₂ released (Fig 8a, 10c).
426 An fS_2 too high will not be compatible with the observed XCO₂/XSO₂ ratio, in particular if the
427 majority of outgassed sulphur is sourced from magma of deep mantle provenance (Fig 11). The
428 amount of fluid in the reservoir is also critical if the final fluid released is to have an XH₂O/XSO₂
429 lower than XCO₂/XSO₂, as observed. According to our calculations, amounts of fluid significantly
430 below 5 wt% (at 300 MPa) cannot satisfy this constraint (Fig. 10). An XH₂O/XSO₂ ratio of 22 and
431 an XCO₂/XSO₂ ratio of 35 requires fO_2 to be ~ NNO+0.6, which is lower than inferred, and which
432 would not sustain elevated S content in the melt (Fig. 6). This illustrates the challenge of delineating
433 conditions that satisfy all observations. Beyond model uncertainties, such discrepancies may also
434 reflect fractionation of gases during magma ascent, either near the surface (Burton et al., 2023), or
435 deeper in the plumbing system. Uncertainties in magma's fO_2 remain large also and more work is
436 needed to refine La Palma redox state, given the importance of this parameter on S behaviour. An
437 additional caveat is that observed gases at La Palma likely represent the mixture of volatiles sourced
438 from magma already stagnating in the reservoir, possibly years before the eruption (e.g., Day et al.,
439 2022; Andujar et al., submitted), as well as mantle-derived volatile-rich magmas (Zanon et al.,
440 2024; Dayton et al., 2024), injected shortly before or during eruption. Such processes, likely in
441 play, are not captured by our treatment.

442

443 **6. Conclusions**

444 We have shown that the composition of the residual glass as well as the phase relationships and
445 their proportions are primarily influenced by oxygen fugacity, but also by the amount of sulphur in
446 the system, though to a lesser extent. Similarly, our experiments emphasise the considerable
447 influence of fO_2 on the solubility of S in silicate melts (Figs. 5,6). Between NNO-0.48 and
448 NNO1.34, the maximum S concentration in the residual glass is 0.2 ± 0.01 wt%, while at oxygen
449 fugacity above NNO+2.38, the maximum value is 0.7–0.8 wt%. These limits are imposed by the
450 buffering effect of sulphide/sulphate phases in addition to the fluid.

451 Modelling of the fluid phase composition using an MRK equation of state for fluid and the models
452 of Lesne et al. (2015) and Jiménez-Mejías et al. (2021) for volatile solubilities, shows that the S
453 content of the fluid lies between 1 and 10 wt%, depending on fS_2 . Overall, the calculations show
454 that in order to expel 2-4 Mt of SO_2 , the pre-eruptive magma must have had a fS_2 at the 0.1 MPa
455 level (Fig. 11a) with an fO_2 above NNO, in general agreement with the oxidised character inferred
456 for hot spot basalts (Moussallam et al., 2019), and coexisted with a significant amount of exsolved
457 fluid in the crustal reservoir.

458

459

460 **Acknowledgement**

461 Acknowledge support from both LabEx VOLTAIRE (ANR-10-LABX-100-01) and EquipEx
462 PLANEX (ANR-11-EQPX-0036) projects. We thank Mike Burton and an anonymous reviewer for
463 their constructive comments which helped to improve significantly the manuscript, as well as the
464 editorial handling of Sonia Calvari.

- 467 Albarède, F., 1996. Introduction to geochemical modeling, 1. paperback ed. (with corr.). ed. Cambridge
468 Univ. Press, Cambridge.
- 469 Albertos, V.T., Hernández, P.A., Melián, G.V., Álvarez Díaz, A.J., Martín-Lorenzo, A., Padrón, E., Pérez,
470 N.M., 2023. Diffuse CO₂ and H₂S degassing from Tajogaite volcanic cone, La Palma, Canary
471 Islands (other). oral. <https://doi.org/10.5194/egusphere-egu23-9916>
- 472 Andújar, et al., 2024. Evolution of the crustal reservoir feeding La Palma 2021 eruption. Insights from
473 phase equilibrium experiments and petrologically derived time scales. *J. Volcanol. Geotherm. Res.*
474 submitted
- 475 Arce, J.L., Walker, J., Keppie, J.D., 2014. Petrology of two contrasting Mexican volcanoes, the
476 Chiapanecan (El Chichón) and Central American (Tacaná) volcanic belts: the result of rift- *versus*
477 subduction-related volcanism. *Int. Geol. Rev.* 56, 501–524.
478 <https://doi.org/10.1080/00206814.2013.879375>
- 479 Bonadonna, C., Pistolesi, M., Biass, S., Voloschina, M., Romero, J., Coppola, D., Folch, A., D’Auria, L.,
480 Martín-Lorenzo, A., Dominguez, L., Pastore, C., Reyes Hardy, M., Rodríguez, F., 2022. Physical
481 Characterization of Long-Lasting Hybrid Eruptions: The 2021 Tajogaite Eruption of Cumbre
482 Vieja (La Palma, Canary Islands). *J. Geophys. Res. Solid Earth* 127, e2022JB025302.
483 <https://doi.org/10.1029/2022JB025302>
- 484 Boulliung, J., Wood, B.J., 2023. Sulfur oxidation state and solubility in silicate melts. *Contrib. Mineral.*
485 *Petrol.* 178, 56. <https://doi.org/10.1007/s00410-023-02033-9>
- 486 Burgisser, A., Scaillet, B., 2007. Redox evolution of a degassing magma rising to the surface. *Nature* 445,
487 194–197. <https://doi.org/10.1038/nature05509>
- 488 Burton, M., Aiuppa, A., Allard, P., Asensio-Ramos, M., Cofrades, A.P., La Spina, A., Nicholson, E.J.,
489 Zanon, V., Barrancos, J., Bitetto, M., Hartley, M., Romero, J.E., Waters, E., Stewart, A.,
490 Hernández, P.A., Lages, J.P., Padrón, E., Wood, K., Esse, B., Hayer, C., Cyrzan, K., Rose-Koga,
491 E.F., Schiavi, F., D’Auria, L., Pérez, N.M., 2023. Exceptional eruptive CO₂ emissions from intra-
492 plate alkaline magmatism in the Canary volcanic archipelago. *Commun. Earth Environ.* 4, 467.
493 <https://doi.org/10.1038/s43247-023-01103-x>
- 494 Carracedo, J.C., Badiola, E.R., Guillou, H., de La Nuez, J., Perez Torrado, F.J., 2001. Geology and
495 volcanology of la Palma and El Hierro, Western Canaries. *Estud. Geol.-Madr.* 57, 175–273.
- 496 Carroll, M.R., Rutherford, M.J., 1988. Sulfur speciation in hydrous experimental glasses of varying
497 oxidation state; results from measured wavelength shifts of sulfur X-rays. *Am. Mineral.* 73, 845–
498 849.
- 499 Carroll, M.R., Rutherford, M.J., 1985. Sulfide and sulfate saturation in hydrous silicate melts. *J. Geophys.*
500 *Res. Solid Earth* 90. <https://doi.org/10.1029/JB090iS02p0C601>
- 501 Castro, J.M., Feisel, Y., 2022. Author Correction: Eruption of ultralow-viscosity basanite magma at
502 Cumbre Vieja, La Palma, Canary Islands. *Nat. Commun.* 13, 3929.
503 <https://doi.org/10.1038/s41467-022-31649-x>
- 504 Clemente, B., Scaillet, B., Pichevant, M., 2004. The Solubility of Sulphur in Hydrous Rhyolitic Melts. *J.*
505 *Petrol.* 45, 2171–2196. <https://doi.org/10.1093/petrology/egh052>
- 506 D’Auria, L., Koulakov, I., Prudencio, J., Cabrera-Pérez, I., Ibáñez, J.M., Barrancos, J., García-Hernández,
507 R., Martínez Van Dorth, D., Padilla, G.D., Przeor, M., Ortega, V., Hernández, P., Pérez, N.M.,
508 2022. Rapid magma ascent beneath La Palma revealed by seismic tomography. *Sci. Rep.* 12,
509 17654. <https://doi.org/10.1038/s41598-022-21818-9>
- 510 Day, J.M.D., Troll, V.R., Aulinas, M., Deegan, F.M., Geiger, H., Carracedo, J.C., Pinto, G.G., Perez-
511 Torrado, F.J., 2022. Mantle source characteristics and magmatic processes during the 2021 La
512 Palma eruption. *Earth Planet. Sci. Lett.* 597, 117793. <https://doi.org/10.1016/j.epsl.2022.117793>
- 513 Dayton, K., Gazel, E., Wieser, P., Troll, V.R., Carracedo, J.C., La Madrid, H., Roman, D.C., Ward, J.,
514 Aulinas, M., Geiger, H., Deegan, F.M., Gisbert, G., Perez-Torrado, F.J., 2023. Deep magma

515 storage during the 2021 La Palma eruption. *Sci. Adv.* 9, eade7641.
516 <https://doi.org/10.1126/sciadv.ade7641>

517 Dayton, K., Gazel, E., Wieser, P.E., Troll, V.R., Carracedo, J.C., Aulinas, M., Perez-Torrado, F.J., 2024.
518 Magmatic Storage and Volatile Fluxes of the 2021 La Palma Eruption. *Geochem. Geophys.*
519 *Geosystems* 25, e2024GC011491. <https://doi.org/10.1029/2024GC011491>

520 Del Fresno, C., Cesca, S., Klügel, A., Domínguez Cerdeña, I., Díaz-Suárez, E.A., Dahm, T., García-
521 Cañada, L., Meletlidis, S., Milkereit, C., Valenzuela-Malebrán, C., López-Díaz, R., López, C.,
522 2023a. Magmatic plumbing and dynamic evolution of the 2021 La Palma eruption. *Nat. Commun.*
523 14, 358. <https://doi.org/10.1038/s41467-023-35953-y>

524 Del Fresno, C., Cesca, S., Klügel, A., Domínguez Cerdeña, I., Díaz-Suárez, E.A., Dahm, T., García-
525 Cañada, L., Meletlidis, S., Milkereit, C., Valenzuela-Malebrán, C., López-Díaz, R., López, C.,
526 2023b. Magmatic plumbing and dynamic evolution of the 2021 La Palma eruption. *Nat. Commun.*
527 14, 358. <https://doi.org/10.1038/s41467-023-35953-y>

528 Devine, J.D., Gardner, J.E., Brack, H.P., Layne, G.D., Rutherford, M.J., 1995. Comparison of
529 microanalytical methods for estimating H₂O contents of silicic volcanic glasses. *Am. Mineral.*
530 80, 319–328. <https://doi.org/10.2138/am-1995-3-413>

531 Di Carlo, I., Pichavant, M., Rotolo, S.G., Scaillet, B., 2006. Experimental Crystallization of a High-K Arc
532 Basalt: the Golden Pumice, Stromboli Volcano (Italy). *J. Petrol.* 47, 1317–1343.
533 <https://doi.org/10.1093/petrology/egl011>

534 Erdmann, S., Pichavant, M., Gaillard, F., 2024. Mineral-melt vanadium oxybarometry for primitive arc
535 magmas: effect of hydrous melt composition on fO₂ estimates. *Contrib. Mineral. Petrol.* 179, 39.
536 <https://doi.org/10.1007/s00410-024-02113-4>

537 Froese, E., Gunter, A.E., 1976. A note on the pyrrhotite-sulfur vapor equilibrium. *Econ. Geol.* 71, 1589–
538 1594. <https://doi.org/10.2113/gsecongeo.71.8.1589>

539 González, F., Seas, C., Barrientos, Z., Quesada-Acuña, S.G., Mora Amador, R.A., 2019. Poás Volcano
540 Biodiversity, in: Tassi, F., Vaselli, O., Mora Amador, Raul Alberto (Eds.), *Poás Volcano: The*
541 *Pulsing Heart of Central America Volcanic Zone, Active Volcanoes of the World.* Springer
542 International Publishing, Cham, pp. 309–317. https://doi.org/10.1007/978-3-319-02156-0_13

543 González-García, D., Boulesteix, T., Klügel, A., Holtz, F., 2023. Bubble-enhanced basanite–tephrite
544 mixing in the early stages of the Cumbre Vieja 2021 eruption, La Palma, Canary Islands. *Sci. Rep.*
545 13, 14839. <https://doi.org/10.1038/s41598-023-41595-3>

546 Hayer, C., Barrancos, J., Burton, M., Rodríguez, F., Esse, B., Hernández, P., Melián, G., Padrón, E.,
547 Asensio-Ramos, M., Pérez, N., 2022. From up above to down below: Comparison of satellite- and
548 ground-based observations of SO₂ emissions from the 2021 eruption of Cumbre Vieja, La Palma
549 (other). *display*. <https://doi.org/10.5194/egusphere-egu22-12201>

550 Hughes, E.C., Saper, L.M., Liggins, P., O’Neill, H.S.C., Stolper, E.M., 2023. The sulfur solubility
551 minimum and maximum in silicate melt. *J. Geol. Soc.* 180, jgs2021-125.

552 Jiménez-Mejías, M., Andújar, J., Scaillet, B., Casillas, R., 2021. Experimental determination of H₂O and
553 CO₂ solubilities of mafic alkaline magmas from Canary Islands. *Comptes Rendus Géoscience*
554 353, 289–314. <https://doi.org/10.5802/crgeos.84>

555 Jugo, P.J., 2004. An Experimental Study of the Sulfur Content in Basaltic Melts Saturated with
556 Immiscible Sulfide or Sulfate Liquids at 1300 C and 1{middle dot}0 GPa. *J. Petrol.* 46, 783–798.
557 <https://doi.org/10.1093/petrology/egh097>

558 Jugo, P.J., Luth, R.W., Richards, J.P., 2005. Experimental data on the speciation of sulfur as a function of
559 oxygen fugacity in basaltic melts. *Geochim. Cosmochim. Acta* 69, 497–503.
560 <https://doi.org/10.1016/j.gca.2004.07.011>

561 Keppler, H., 1999. Experimental Evidence for the Source of Excess Sulfur in Explosive Volcanic
562 Eruptions. *Science* 284, 1652–1654. <https://doi.org/10.1126/science.284.5420.1652>

563 Lesne, P., Scaillet, B., Pichavant, M., 2015. The solubility of sulfur in hydrous basaltic melts. *Chem. Geol.*
564 418, 104–116. <https://doi.org/10.1016/j.chemgeo.2015.03.025>

565 Liu, Y., Samaha, N.-T., Baker, D.R., 2007. Sulfur concentration at sulfide saturation (SCSS) in magmatic
566 silicate melts. *Geochim. Cosmochim. Acta* 71, 1783–1799.
567 <https://doi.org/10.1016/j.gca.2007.01.004>

568 Lo Forte, F.M., Schiavi, F., Rose-Koga, E.F., Rotolo, S.G., Verdier-Paoletti, M., Aiuppa, A., Zanon, V.,
569 2024. High CO₂ in the mantle source of ocean island basanites. *Geochim. Cosmochim. Acta* 368,
570 93–111. <https://doi.org/10.1016/j.gca.2024.01.016>

571 Luhr, J.F., 1990. Experimental Phase Relations of Water- and Sulfur-Saturated Arc Magmas and the 1982
572 Eruptions of El Chichón Volcano. *J. Petrol.* 31, 1071–1114.
573 <https://doi.org/10.1093/petrology/31.5.1071>

574 Moretti, R., Ottonello, G., 2005. Solubility and speciation of sulfur in silicate melts: The Conjugated
575 Toop-Samis-Flood-Grjotheim (CTSFG) model. *Geochim. Cosmochim. Acta* 69, 801–823.
576 <https://doi.org/10.1016/j.gca.2004.09.006>

577 Moune, S., Holtz, F., Botcharnikov, R.E., 2009. Sulphur solubility in andesitic to basaltic melts:
578 implications for Hekla volcano. *Contrib. Mineral. Petrol.* 157, 691–707.
579 <https://doi.org/10.1007/s00410-008-0359-0>

580 Moussallam, Y., Edmonds, M., Scaillet, B., Peters, N., Gennaro, E., Sides, I., Oppenheimer, C., 2016. The
581 impact of degassing on the oxidation state of basaltic magmas: A case study of Kīlauea volcano.
582 *Earth Planet. Sci. Lett.* 450, 317–325. <https://doi.org/10.1016/j.epsl.2016.06.031>

583 O'Neill, H.St.C., 2021. The Thermodynamic Controls on Sulfide Saturation in Silicate Melts with
584 Application to Ocean Floor Basalts, in: Moretti, R., Neuville, D.R. (Eds.), *Geophysical*
585 *Monograph Series*. Wiley, pp. 177–213. <https://doi.org/10.1002/9781119473206.ch10>

586 Oppenheimer, C., Fischer, T.P., Scaillet, B., 2014. Volcanic Degassing: Process and Impact, in: *Treatise*
587 *on Geochemistry*. Elsevier, pp. 111–179. <https://doi.org/10.1016/B978-0-08-095975-7.00304-1>

588 Pérez, I.C., 2022. Relative velocity variations curves. <https://doi.org/10.5281/ZENODO.6678861>

589 Sandoval-Velasquez, A., Rizzo, A.L., Casetta, F., Ntaflos, T., Aiuppa, A., Alonso, M., Padrón, E.,
590 Pankhurst, M.J., Mundl-Petermeier, A., Zanon, V., Pérez, N.M., 2023. The noble gas signature of
591 the 2021 Tajogaite eruption (La Palma, Canary Islands). *J. Volcanol. Geotherm. Res.* 443,
592 107928. <https://doi.org/10.1016/j.jvolgeores.2023.107928>

593 Scaillet, B., Clemente, B., Evans, B.W., Pichavant, M., 1998. Redox control of sulfur degassing in silicic
594 magmas. *J. Geophys. Res. Solid Earth* 103, 23937–23949. <https://doi.org/10.1029/98JB02301>

595 Scaillet, B., Evans, B.W., 1999. The 15 June 1991 Eruption of Mount Pinatubo. I. Phase Equilibria and
596 Pre-eruption P-T-fO₂-fH₂O Conditions of the Dacite Magma. *J. Petrol.* 40, 381–411.
597 <https://doi.org/10.1093/petroj/40.3.381>

598 Scaillet, B., Luhr, J., Carroll, M.R., 2003. Petrological and volcanological constraints on volcanic sulfur
599 emissions to the atmosphere. *Geophys. Monogr.-Am. Geophys. Union* 139, 11–40.

600 Scaillet, B., Pichavant, M., Roux, J., Humbert, G., Lefevre, A., 1992. Improvements of the Shaw
601 membrane technique for measurement and control of fH₂ at high temperatures and pressures. *Am.*
602 *Mineral.* 77, 647–655.

603 Sisson, T.W., Grove, T.L., 1993. Experimental investigations of the role of H₂O in calc-alkaline
604 differentiation and subduction zone magmatism. *Contrib. Mineral. Petrol.* 113, 143–166.
605 <https://doi.org/10.1007/BF00283225>

606 Taylor, J.R., Wall, V.J., Pownceby, M.I., 1992. The calibration and application of accurate redox sensors.
607 *Am. Mineral.* 77, 284–295.

608 Ubide, T., Márquez, Á., Ancochea, E., Huertas, M.J., Herrera, R., Coello-Bravo, J.J., Sanz-Mangas, D.,
609 Mulder, J., MacDonald, A., Galindo, I., 2023. Discrete magma injections drive the 2021 La Palma
610 eruption. *Sci. Adv.* 9, eadg4813. <https://doi.org/10.1126/sciadv.adg4813>

611 Whitney, J.A., 1984. Fugacities of sulfurous gases in pyrrhotite-bearing silicic magmas. *Am. Mineral.* 69,
612 68–78.

613 Zanon, V., D'Auria, L., Schiavi, F., Cyrzan, K., Pankhurst, M.J., 2024. Toward a near real-time magma
614 ascent monitoring by combined fluid inclusion barometry and ongoing seismicity. *Sci. Adv.* 10,
615 eadi4300. <https://doi.org/10.1126/sciadv.adi4300>

